

# Active 6D Pose Estimation for Textureless Objects using Multi-View RGB Frames

The International Journal of Robotics Research  
XX(X):1–19  
©The Author(s) 2025  
Reprints and permission:  
sagepub.co.uk/journalsPermissions.nav  
DOI: 10.1177/ToBeAssigned  
www.sagepub.com/

SAGE

Jun Yang<sup>1,2</sup>, Wenjie Xue<sup>2</sup>, Sahar Ghavidel<sup>2</sup> and Steven L. Waslander<sup>1</sup>

## Abstract

Estimating the 6D pose of textureless objects from RGB images is an important problem in robotics. Due to appearance ambiguities, rotational symmetries, and severe occlusions, single-view based 6D pose estimators are still unable to handle a wide range of objects, motivating research towards multi-view pose estimation and next-best-view prediction that addresses these limitations. In this work, we propose a comprehensive active perception framework for estimating the 6D poses of textureless objects using only RGB images. Our approach is built upon a key idea: decoupling the 6D pose estimation into a sequential two-step process can greatly improve both accuracy and efficiency. First, we estimate the 3D translation of each object, resolving scale and depth ambiguities inherent to RGB images. These estimates are then used to simplify the subsequent task of determining the 3D orientation, which we achieve through canonical scale template matching. Building on this formulation, we then introduce an active perception strategy that predicts the next best camera viewpoint to capture an RGB image, effectively reducing object pose uncertainty and enhancing pose accuracy. We evaluate our method on the public ROBI dataset as well as on a transparent object dataset that we created. When evaluated using the same camera viewpoints, our multi-view pose estimation significantly outperforms state-of-the-art approaches. Furthermore, by leveraging our next-best-view strategy, our method achieves high object pose accuracy with substantially fewer viewpoints than heuristic-based policies.

## Keywords

6D Object Pose, Multi-View Optimization, Active Vision, Deep Learning

## 1 Introduction

Texture-less rigid objects occur frequently in industrial environments and are of significant interest in many robotic applications. The task of 6D pose estimation aims to detect objects of known geometry and estimate their 6DoF (Degree of Freedom) poses, i.e., 3D translations and 3D orientations, with respect to a global coordinate frame. In robotic manipulation tasks, accurate object poses are required for path planning and grasp execution (Song et al. 2017; Tremblay et al. 2018; Wang et al. 2019; Deng et al. 2020). For robotic navigation, 6D object poses provide useful information to the robot for localization and obstacle avoidance (Salas-Moreno et al. 2013; Fu et al. 2021; Merrill et al. 2022; Wang et al. 2021; Liao et al. 2024).

Due to the absence of appearance features, 6D pose estimation for textureless objects has traditionally been addressed using depth data (Drost et al. 2010; Bui et al. 2018; Gao et al. 2020, 2021; Cai et al. 2022; Li and Stamos 2023) or RGB-D images (Doumanoglou et al. 2016; Wang et al. 2019; Wada et al. 2020; He et al. 2020; Tian et al. 2020; Saadi et al. 2021; Li and Schoellig 2023). These methods demonstrate strong pose estimation performance when high-quality depth data is available. However, despite significant advances in depth acquisition technology, commodity-grade depth cameras still produce inaccurate depth maps, often suffering from errors or missing data when surfaces are glossy or dark (Chai et al. 2020; Yang and Waslander 2022; Yang et al. 2024), or when the object is translucent or transparent (Sajjan et al. 2020; Liu et al. 2020; Xu

et al. 2021). These depth limitations can severely degrade object pose estimation performance. Therefore, RGB-based approaches have received a lot of attention over the past decade as a promising alternative (Hinterstoisser et al. 2011; Brachmann et al. 2016).

Due to the myriad advances in deep learning over the last decade, some learning-based approaches have recently been shown to significantly improve object pose estimation performance using only RGB images (Kehl et al. 2017; Xiang et al. 2018; Sundermeyer et al. 2018; Peng et al. 2019; Hodan et al. 2020; He et al. 2023; Xu et al. 2024). However, due to the inherent scale, depth, and perspective ambiguities from a single viewpoint, RGB-based solutions often suffer from low accuracy in the final 6D pose estimation. To this end, recent works leverage multiple RGB views to enhance their pose estimation results (Labbé et al. 2020; Deng et al. 2021; Shugurov et al. 2021; Fu et al. 2021; Maninis et al. 2022; Merrill et al. 2022; Haugaard and Iversen 2023). Although fusing multi-view information can enhance overall performance, addressing challenges such as appearance ambiguities, rotational symmetries, and

<sup>1</sup>University of Toronto Institute for Aerospace Studies and Robotics Institute, ON, Canada

<sup>2</sup>Epson Canada Ltd, ON, Canada

## Corresponding author:

Jun Yang, University of Toronto Institute for Aerospace Studies, M3H 5T6, ON, Canada.

Email: jun.yang@robotics.utoronto.ca

occlusions remains difficult. Additionally, even when multi-view fusion mitigates some of these issues, relying on a large number of viewpoints is often impractical for many real-world applications, such as robotic manipulation.

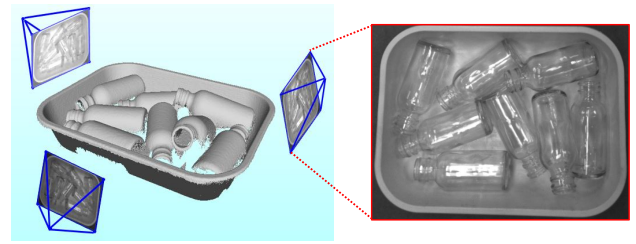
To address these challenges, we present a comprehensive framework for both object pose estimation and next-best-view prediction using multi-view RGB images. First, we introduce a multi-view object pose estimation method that decouples the 6D pose estimation into a two-step process: we first estimate the 3D translation, followed by the 3D orientation of each object. This decoupled approach resolves scale and depth ambiguities from single RGB images, using the translation estimate to simplify the orientation estimation problem. This decoupled formulation first resolves scale and depth ambiguities in single RGB images, then uses these estimates to simplify object orientation estimation in the second stage. To address the multi-modal nature of orientation space, we develop an optimization scheme that accounts for object symmetries and counteracts measurement uncertainties. The second part of our framework focuses on next-best-view (NBV) prediction, which builds upon the proposed multi-view pose estimator. We introduce an information-theoretic approach to quantify object pose uncertainty. In each NBV iteration, we predict the expected object pose uncertainty for each potential viewpoint and select the next camera viewpoint that minimizes this uncertainty, ensuring more informative RGB measurements are collected.

We conduct extensive experiments on the ROBI dataset (Yang et al. 2021) and a transparent object dataset that we created. Additionally, to support network training, we generated a large-scale synthetic dataset incorporating objects from both the ROBI dataset and our transparent dataset. Our approach significantly outperforms state-of-the-art RGB-based methods. When compared to depth-based methods, it achieves comparable performance, despite relying solely on RGB images. Furthermore, compared to baseline viewpoint selection strategies, our next-best-view strategy achieves high object pose accuracy while requiring significantly fewer viewpoints.

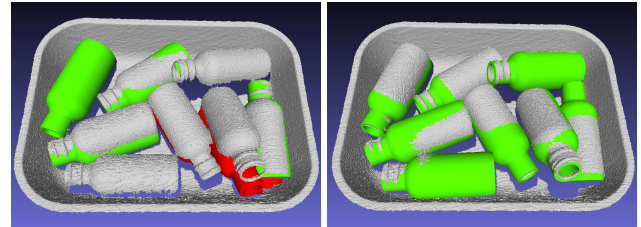
Our work makes the following key contributions.

- We propose a novel 6D object pose estimation framework that decouples the problem into a sequential two-step process. This process resolves the depth ambiguities from RGB frames and greatly improves the estimate of orientation parameters.
- Building on our proposed pose estimator, we introduce an information-theoretic active vision strategy that optimizes object pose accuracy by selecting the next-best camera viewpoint.
- We introduce a multi-view dataset of transparent objects, specifically designed to evaluate 6D pose estimation for transparent parts in cluttered and occluded bin scenarios.
- To support network training, we create a large-scale synthetic dataset that includes all parts from both the ROBI dataset and our transparent object dataset.

It is important to note that this work substantially extends our previous conference paper (Yang et al. 2023b), with the following improvements:



(a) Input: Multi-View RGB Images.



(b) Results from CosyPose.

(c) Results from Ours.

**Figure 1.** 6D object pose estimation using multi-view acquired RGB images. (a) The input multi-view RGB images with known camera poses. (b) The pose estimation results using CosyPose and PVNet. (c) The pose estimation results using our approach. The green and red colors represent correct and incorrect pose estimations, respectively.

- **Improved Orientation Estimation.** To enhance object orientation estimation, we introduce a new head into the neural network architecture that extracts per-frame object edge maps, which serve as more accurate and consistent shape inputs for the object orientation estimator.
- **Active Vision.** We extend our previous approach by integrating an active vision strategy that selects the next-best-view to improve the object pose accuracy.
- **Transparent Object Dataset.** The creation of a transparent object dataset ensures that our method is evaluated under real-world, challenging conditions, further demonstrating its effectiveness.
- **Synthetic Dataset.** The generated large-scale synthetic dataset will provide researchers with a comprehensive benchmark for training and making fair comparisons on ROBI and our transparent object dataset.

The rest of the paper is organized as follows. Section 2 reviews the relevant literature. Section 3 formulates the multi-view object pose estimation problem. Section 4 describes the next-best-view prediction approach. Section 5 presents the experimental results, and Section 6 concludes the paper.

## 2 Related Works

### 2.1 Object Pose Estimation from a Single RGB Image

Many approaches have been presented in recent years to address the pose estimation problem for texture-less objects using only RGB images. Due to the lack of appearance features, traditional methods usually tackle the problem via holistic template matching techniques (Hinterstoisser et al. 2011; Imperoli and Pretto 2015; Hodař et al. 2015), but are susceptible to failure due to scale change and

in cluttered environments. More recently, deep learning techniques, such as convolutional neural networks (CNNs), have been employed to overcome these challenges (Kehl et al. 2017; Xiang et al. 2018; Sundermeyer et al. 2018; Li et al. 2018; Peng et al. 2019; Hodan et al. 2020; He et al. 2023; Xu et al. 2024). Pioneering methods such as SSD-6D (Kehl et al. 2017), PoseCNN (Xiang et al. 2018), and AAE (Sundermeyer et al. 2018) developed CNN architectures for estimating 6D object poses from a single RGB image. Some recent works leverage deep neural networks to first predict 2D object keypoints (Rad and Lepetit 2017; Pavlakos et al. 2017; Peng et al. 2019; He et al. 2023; Xu et al. 2024) or dense 2D-3D correspondences (Zakharov et al. 2019; Park et al. 2019; Hodan et al. 2020; Haugaard and Buch 2022), and then compute the pose through 2D-3D correspondences with a Perspective-n-Point (PnP) algorithm (Lepetit et al. 2009). Although these methods excel in 2D metrics, their accuracy in estimating final 6D poses is limited by inherent ambiguities in scale and depth, as well as occlusions from a single viewpoint. As a result, depth data is often required to refine the object pose (Rusinkiewicz and Levoy 2001; Deng et al. 2021; Schmidt et al. 2014; Zhang and Cao 2019; Yang et al. 2024).

## 2.2 Object Pose Estimation from Multiple Viewpoints

Multi-view approaches are designed to address the scale and depth ambiguities that commonly occur in single-viewpoint scenarios, thereby improving the accuracy of estimated poses. Traditional methods rely on local features (Eidenberger and Scharinger 2010; Collet and Srinivasa 2010) but struggle to handle textureless objects. More recently, the problem of multi-view object pose estimation has been revisited with neural networks. These approaches employ an offline, batch-based optimization framework, where all frames are processed simultaneously to produce a consistent interpretation of the scene (Kundu et al. 2018; Labbé et al. 2020; Liu et al. 2020; Shugurov et al. 2021; Haugaard and Iversen 2023; Chen et al. 2023). Other approaches address the multi-view pose estimation problem in an online manner. These works estimate camera poses and object poses simultaneously, known as object-level SLAM (Yang and Scherer 2019; Fu et al. 2021; Wu et al. 2020; Merrill et al. 2022), or estimate object poses with known camera poses (Deng et al. 2020, 2021; Maninis et al. 2022). Although these methods demonstrate performance improvements with only RGB images, they still face challenges in handling object scales, rotational symmetries, and measurement uncertainties. Using per-frame neural network predictions as measurements, our approach resolves depth and scale ambiguities through a decoupled formulation. It also explicitly addresses rotational symmetries and measurement uncertainties within an incremental online framework.

## 2.3 Active Vision

Active vision (Aloimonos et al. 1988; Chen et al. 2011; Bajcsy et al. 2018), or more specifically Next-Best-View (NBV) prediction (Connolly 1985), refers to actively

manipulating the camera viewpoint to obtain the maximum information in the next frame for the required task. Active vision has received a lot of attention from the robotics community and has been employed in many applications, such as robot manipulation (Morrison et al. 2019; Breyer et al. 2022), calibration (Rebello et al. 2017; Yang et al. 2023a; Choi et al. 2023; Xu et al. 2023), object pose estimation (Eidenberger and Scharinger 2010; Wu et al. 2015; Doumanoglou et al. 2016; Sock et al. 2020; Yang et al. 2024), 3D reconstruction (Isler et al. 2016; Forster et al. 2014; Yang and Waslander 2022) and localization (Davison and Murray 2002; Zhang and Scaramuzza 2018, 2019). The next-best-view selection is often achieved by finding the viewpoint that maximizes the information gain or minimizes the expected entropy (Rebello et al. 2017; Yang et al. 2023a; Choi et al. 2023; Xu et al. 2023; Doumanoglou et al. 2016; Zhang and Scaramuzza 2018, 2019). To estimate 6D object poses, Doumanoglou et al. first present a single-shot object pose estimation approach based on Hough Forests (Doumanoglou et al. 2016). The next-best-view is predicted by exploiting the capability of Hough Forests to compute the entropy. To eliminate reliance on the Hough Forests, recent studies show that the next-best-view can be achieved by maximizing the Fisher information of the robot state parameters (Forster et al. 2014; Zhang and Scaramuzza 2018, 2019; Yang et al. 2023a, 2024). For example, in robot localization, the authors in (Zhang and Scaramuzza 2018, 2019) use the Fisher information maximization to find highly informative trajectories and achieve high localization accuracy.

## 3 6D Pose Estimation using Multi-View Optimization

### 3.1 Problem Formulation

Given a 3D object model and multi-view images, the goal of 6D object pose estimation is to estimate the rigid transformation  $\mathbf{T}_{wo} \in SE(3)$  that maps the object model frame  $O$  to a global (world) frame  $W$ . We assume that the camera poses  $\mathbf{T}_{wc} \in SE(3)$  relative to the world frame are known. These can be determined through robot forward kinematics and eye-in-hand calibration (Tsai and Lenz 1989) when the camera is mounted on the end-effector of a robotic arm, or through off-the-shelf SLAM methods (Klein and Murray 2007; Mur-Artal et al. 2015) for hand-held cameras.

Given measurements  $\mathbf{Z}_{1:k}$  up to viewpoint  $k$ , we aim to estimate the posterior distribution of the 6D object pose  $P(\mathbf{R}_{wo}, \mathbf{t}_{wo} | \mathbf{Z}_{1:k})$ . Direct computation of this distribution is typically infeasible because object translation  $\mathbf{t}_{wo}$  and orientation  $\mathbf{R}_{wo}$  follow distinct distributions. Specifically, the translation distribution  $P(\mathbf{t}_{wo})$  is straightforward and expected to be unimodal. In contrast, the distribution for object orientation  $P(\mathbf{R}_{wo})$  is more complex, influenced by uncertainties related to object shape symmetries, appearance ambiguities, and potential occlusions. Inspired by (Deng et al. 2021), we decouple the pose posterior  $P(\mathbf{R}_{wo}, \mathbf{t}_{wo} | \mathbf{Z}_{1:k})$  into:

$$P(\mathbf{R}_{wo}, \mathbf{t}_{wo} | \mathbf{Z}_{1:k}) = P(\mathbf{R}_{wo} | \mathbf{Z}_{1:k}, \mathbf{t}_{wo}) P(\mathbf{t}_{wo} | \mathbf{Z}_{1:k}), \quad (1)$$

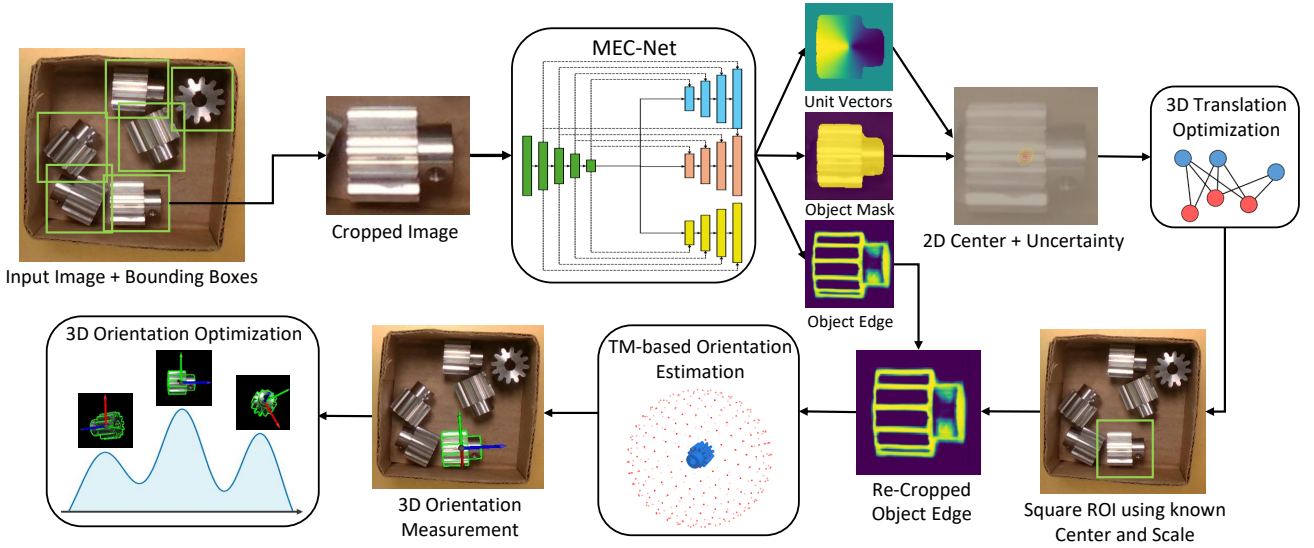


**Figure 2.** An overview of the proposed multi-view object pose estimation pipeline with a two-step optimization formulation. We decouple the 6D pose estimation into a sequential two-step process: first estimating the 3D translation, followed by the 3D orientation of each object. At each viewpoint, our SEC-Net generates the object’s 2D center, mask, and edge map. Leveraging these estimates, we first calculate the 3D translation through multi-view optimization. This translation estimation provides the object’s scale and center within the image, allowing us to re-crop the ROI of object’s edge map and obtain the per-frame object orientation measurement. The final object orientation is finally determined through a max-mixture optimization.

where  $P(\mathbf{t}_{wo}|\mathbf{Z}_{1:k})$  can be formulated as a unimodal Gaussian distribution,  $\mathcal{N}(\mathbf{t}_{wo}|\mu, \Sigma)$  and  $P(\mathbf{R}_{wo}|\mathbf{Z}_{1:k}, \mathbf{t}_{wo})$  is the orientation distribution conditioned on the input images  $\mathbf{Z}_{1:k}$  and the 3D translation  $\mathbf{t}_{wo}$ . To represent the complex orientation uncertainties, we follow a similar approach to (Eidenberger and Scharinger 2010) and model  $P(\mathbf{R}_{wo}|\mathbf{Z}_{1:k}, \mathbf{t}_{wo})$  as a mixture of Gaussian distributions:

$$P(\mathbf{R}_{wo}|\mathbf{Z}_{1:k}, \mathbf{t}_{wo}) = \sum_{i=1}^N w_i \mathcal{N}(\mathbf{R}_{wo}|\mu_i, \Sigma_i), \quad (2)$$

which consists of  $N$  Gaussian components, where  $w_i$  is the weight of the  $i^{\text{th}}$  component, and  $\mu_i$  and  $\Sigma_i$  are its mean and covariance, respectively.

Our proposed decoupling formulation implies a useful correlation between the object’s translation and orientation in the image domain. The 3D translation estimation  $\mathbf{t}_{wo}$  is independent of the object’s orientation and encodes its center and scale information. By applying the camera pose  $\mathbf{T}_{wc,k}$  at frame  $k$ , the estimated 3D translation  $\mathbf{t}_{co,k}$  under the camera coordinate provides the scale and 2D center of the object in the image. Using these estimates, the per-frame object orientation measurement  $\mathbf{R}_{co,k}$  can be estimated from its visual appearance in the image. With this formulation, our multi-view framework consists of two main steps, as summarized in Figure 2.

To implement this formulation, a key step in our framework is estimating per-frame measurements using a neural network, which are then integrated into our two-step optimization process. The network outputs the object’s 2D edge map, segmentation mask, and the 2D projection of its 3D center. We refer to our network as **MEC-Net** (Mask, Edge, Center Network) for the remainder of this paper. With these estimates, we proceed to the first step (Section 3.2), where we estimate the 3D translation  $\mathbf{t}_{wo}$  by minimizing the

2D re-projection error across camera viewpoints. Using the estimated 3D translation  $\mathbf{t}_{wo}$ , the second step (Section 3.3) involves re-cropping an orientation-independent Region of Interest (ROI) from each object’s edge map, based on the estimated scale. This ROI is then fed into an orientation estimator (Hinterstoisser et al. 2011) to obtain the per-frame 3D orientation measurement  $\mathbf{R}_{co,k}$ . The final object orientation  $\mathbf{R}_{wo}$  is determined through an optimization approach that explicitly accounts for shape symmetries and incorporates a max-mixture formulation (Olson and Agarwal 2013; Fu et al. 2021) to mitigate uncertainties arising from per-frame orientation estimates.

### 3.2 3D Translation Estimation

As illustrated in Figure 3, the 3D translation  $\mathbf{t}_{wo}$  represents the coordinate of the object model origin in the world frame. Given that the camera pose  $\mathbf{T}_{wc}$  is known, this is equivalent to solving for the translation from the object model origin to the camera optical center,  $\mathbf{t}_{co} = [t_x, t_y, t_z]^T$ . Given an RGB image from an arbitrary camera viewpoint, the translation  $\mathbf{t}_{co}$  can be recovered by the following back-projection, assuming a pinhole camera model,

$$\mathbf{t}_{co} = \begin{bmatrix} t_x \\ t_y \\ t_z \end{bmatrix} = \begin{bmatrix} \frac{u_x - c_x}{f_x} t_z \\ \frac{u_y - c_y}{f_y} t_z \\ t_z \end{bmatrix}, \quad (3)$$

where  $f_x$  and  $f_y$  denote the camera focal lengths, and  $[c_x, c_y]^T$  is the principal point. We define  $\mathbf{u} = [u_x, u_y]^T$  as the 2D projection of the object model origin  $O$  and refer to it as the 2D center of the object in the rest of the paper. If the object center  $\mathbf{u}$  is localized in the image and the depth  $t_z$  to the object center is estimated, then  $\mathbf{t}_{co}$  (or  $\mathbf{t}_{wo}$ ) can be recovered. In our framework, we use MEC-Net to predict the 2D object center  $\mathbf{u}$  for each frame and estimate the depth  $t_z$  through a multi-view optimization formulation.

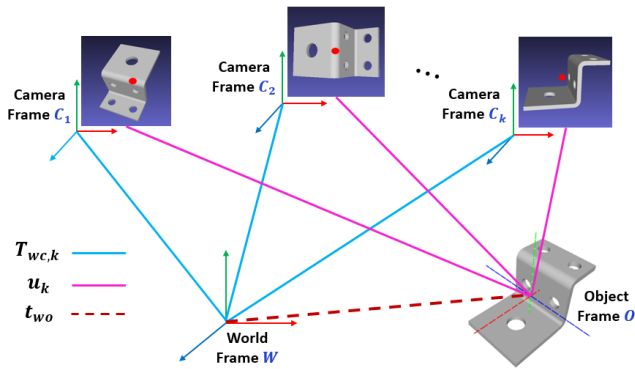


**Figure 3.** Illustration of the object, world, and camera coordinate frames. The 3D translation  $\mathbf{t}_{wo}$  is the coordinate of the object model origin in the world coordinate frame. We can estimate the translation by localizing the per-frame 2D center of the object,  $\mathbf{u}_k$ , and minimizing the re-projection errors with known camera poses  $\mathbf{T}_{wc,k}$ .

Our MEC-Net architecture is shown in the upper part of Figure 2 and is based on PoseCNN (Xiang et al. 2018) and PVNet (Peng et al. 2019). To handle multiple instances within the scene, we first employ YOLOv8 (Redmon et al. 2016) to detect 2D bounding boxes of the objects. These detections are then cropped and resized to 128x128 before being passed to the network. To estimate the object 2D center, the MEC-Net first predicts pixel-wise binary labels and a 2D vector field towards the object center. A RANSAC-based voting scheme is then applied to compute the mean  $\mathbf{u}_k$  and covariance  $\Sigma_{\mathbf{u},k}$  of the object center at frame  $k$ . For more details on object center estimation, we refer the reader to (Xiang et al. 2018; Peng et al. 2019).

Given a sequence of measurements, we estimate the object’s 3D translation  $\mathbf{t}_{wo}$  using a maximum likelihood estimation (MLE) formulation. Assuming a unimodal Gaussian error model, we solve the problem via nonlinear least squares (NLLS) optimization. The optimization is formulated by creating measurement residuals that constrain the object translation  $\mathbf{t}_{wo}$  to the object center  $\mathbf{u}_k$ , its covariance  $\Sigma_{\mathbf{u},k}$ , and known camera pose  $\mathbf{T}_{wc,k}$  at viewpoint  $k$ ,

$$\mathbf{r}_k(\mathbf{t}_{wo}) = \pi(\mathbf{T}_{wc,k}^{-1} \mathbf{t}_{wo}) - \mathbf{u}_k, \quad (4)$$

where  $\pi$  denotes the perspective projection function. The full problem then becomes the minimization of the cost function  $L$  across all viewpoints,

$$L = \sum_k \mathbf{r}_k^T \Sigma_{\mathbf{u},k}^{-1} \mathbf{r}_k, \quad (5)$$

where  $\Sigma_{\mathbf{u},k}$  is the covariance matrix for the object center  $\mathbf{u}_k$ . We initialize each object’s translation  $\mathbf{t}_{wo}$  from two camera viewpoints. For the  $k^{\text{th}}$  camera viewpoint,  $\mathbf{T}_{wc,k}$ , we perform object association based on epipolar geometry constraints and the previously estimated translation  $\mathbf{t}_{wo,1:k-1}$  up to viewpoint  $k-1$ . Detections that are not associated with any existing objects are initialized as new objects.

We solve the NLLS problem (Equation 4 and 5) using an iterative Gauss-Newton procedure:

$$(\mathbf{J}_{\mathbf{t}_{wo}}^T \Sigma_{\mathbf{u}}^{-1} \mathbf{J}_{\mathbf{t}_{wo}}) \delta \mathbf{t}_{wo} = \mathbf{J}_{\mathbf{t}_{wo}}^T \Sigma_{\mathbf{u}}^{-1} \mathbf{r}(\mathbf{t}_{wo}), \quad (6)$$

where the stacked Jacobian matrix,  $\mathbf{J}_{\mathbf{t}_{wo}}$ , and the stacked measurement covariance matrix,  $\Sigma_{\mathbf{u}}$ , are represented by:

$$\mathbf{J}_{\mathbf{t}_{wo}} = \begin{bmatrix} \mathbf{J}_{\mathbf{t}_{wo},\mathbf{u}_1} \\ \vdots \\ \mathbf{J}_{\mathbf{t}_{wo},\mathbf{u}_K} \end{bmatrix}, \quad \Sigma_{\mathbf{u}} = \begin{bmatrix} \Sigma_{\mathbf{u}_1} & & \\ & \ddots & \\ & & \Sigma_{\mathbf{u}_K} \end{bmatrix} \quad (7)$$

The row-blocks,  $\mathbf{J}_{\mathbf{t}_{wo},\mathbf{u}_k}$ , and  $\Sigma_{\mathbf{u}_k}$  correspond to the Jacobian matrix and measurement covariance matrix for the  $k^{\text{th}}$  viewpoint. The per-frame measurement uncertainty,  $\Sigma_{\mathbf{u}_k}$ , is obtained from our MEC-Net (upper part of Figure 2). The Jacobian matrix,  $\mathbf{J}_{\mathbf{t}_{wo},\mathbf{u}_k}$ , is computed as:

$$\mathbf{J}_{\mathbf{t}_{wo},\mathbf{u}_k} = \frac{\partial \mathbf{u}_k}{\partial \mathbf{t}_{wo}} = \frac{\partial \mathbf{u}_k}{\partial \mathbf{t}_{co,k}} \frac{\partial \mathbf{t}_{co,k}}{\partial \mathbf{t}_{wo}}, \quad (8)$$

where  $\mathbf{t}_{co,k}$  is the 3D translation from the object model origin to the camera optical center at the  $k^{\text{th}}$  viewpoint.

### 3.3 3D Orientation Estimation

The procedure for estimating the object orientation  $\mathbf{R}_{wo}$  is shown in the lower part of Figure 2. Given the per-frame edge map from MEC-Net, we first adopt a template matching (TM)-based approach, LINE-2D (Hinterstoisser et al. 2011), to obtain the per-frame orientation measurement  $\mathbf{R}_{co,k}$ . Measurements from multiple viewpoints are then integrated into an optimization scheme. We handle the rotational symmetries explicitly using the object CAD model. To counteract the measurement uncertainties (e.g., from appearance ambiguities), a max-mixture formulation (Olson and Agarwal 2013; Fu et al. 2021) is employed to recover a globally consistent set of object orientation estimates. Note that the acquisition of the orientation measurement  $\mathbf{R}_{co,k}$  is not limited to the LINE-2D (Hinterstoisser et al. 2011) or TM-based approaches and can be superseded by other holistic methods (Liu et al. 2012; Imperoli and Pretto 2015; Kehl et al. 2017; Sundermeyer et al. 2018).

#### 3.3.1 Per-Frame Orientation Measurement

The process of acquiring the per-frame object orientation measurement,  $\mathbf{R}_{co,k}$ , is illustrated in Figure 4. This process is based on a template-matching (TM)-based approach, LINE-2D (Hinterstoisser et al. 2011). The original LINE-2D method estimates the object’s 3D orientation by matching templates derived from the object’s 3D model. In the offline training stage, LINE-2D renders object templates from a view sphere, with each template represented as a set of sampled edge points (shown in the upper part of Figure 4). At run-time, it first extracts the edge pixels (e.g., using a Sobel filter) from the input RGB image and utilizes the gradient response to find the best matched template, determining the object orientation. A confidence score is computed based on the quality of the match. However, the template matching-based approach suffers from scale change and occlusion problems. Additionally, specular reflections on shiny surfaces can introduce false edges, leading to incorrect matches. To address these issues, we propose two major modifications to the LINE-2D algorithm.

**Predicting object edge map.** To bridge the gap between rendered templates and RoI images, and to reduce the impact

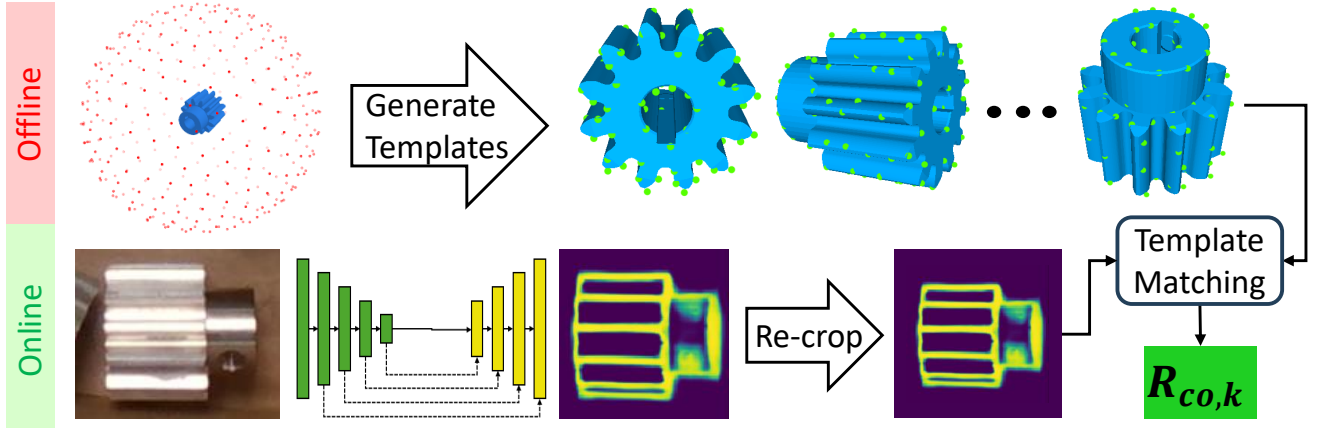


**Figure 4.** The process of acquiring the per-frame object orientation measurement,  $\mathbf{R}_{co,k}$ . This process is based on a template matching (TM)-based approach, LINE-2D. To reduce the gap between rendered templates and ROI images, we introduce a new head into our neural network, MEC-Net (shown in the upper part of Figure 2), and directly generate the object edge map, which serve as the input for template matching.

of spurious edges, we leverage our MEC-Net to directly generate the object’s edge map. As illustrated in Figure 2, we extend our previous approach (Yang et al. 2023b) by adding an extra network head specifically for estimating the object’s 2D edge map. To handle partial occlusion, which is common in real-world scene, we incorporate occlusion augmentation in our training data, similar to the approach used in AAE (Sundermeyer et al. 2018). During training, we treat the edge map as a binary classification task and minimize the cross-entropy loss. At inference, we apply the sigmoid function to map edge pixel values to the range of  $[0, 1]$ , with higher values indicating greater confidence that a pixel belongs to the object edge.

**Handling object scale change.** To address the scale change issue, the original LINE-2D generates object templates at multiple distances and scales, which increases run-time complexity. In contrast, our approach fixes the 3D translation to a canonical centroid distance,  $\mathbf{tr} = [0, 0, z_r]$ . At run-time, given the 3D translation estimate,  $\mathbf{t}_{co} = [x_s, y_s, z_s]$ , from object origin to camera center (obtained from  $\mathbf{t}_{wo}$  and camera pose,  $\mathbf{T}_{wc}$ ), we re-crop the edge map ROI from the image. The ROI size  $l_s$  is determined by:

$$l_s = \frac{z_r}{z_s} l_r, \quad (9)$$

where  $l_r$  and  $z_r$  represent the ROI size and canonical distance during training, respectively. This process is illustrated in Figure 5a. As demonstrated in Figure 5b, when the translation estimate,  $\mathbf{t}_{co}$ , is accurate, the resized edge map ROI will have the same size with the rendered object template at the canonical distance. Note that the ROI is square here and independent of the object’s orientation. Finally, the per-frame measurement of the object orientation,  $\mathbf{R}_{co,k}$ , is obtained by feeding the resized ROI into the LINE-2D orientation estimator.

### 3.3.2 Optimization formulation

Given the multi-view orientation measurements,  $\mathbf{R}_{co,k}$ , we aim to estimate the object’s 3D orientation in the global world frame. Generally, estimating the object’s 3D orientation from a sequence of such measurements can also

be formulated as an MLE problem:

$$\hat{\mathbf{X}} = \operatorname{argmax}_{\mathbf{X}} \prod_k p(\mathbf{z}_k | \mathbf{X}), \quad (10)$$

where  $\mathbf{X}$  denotes the object 3D orientation,  $\mathbf{R}_{wo}$ , to be estimated. The measurement  $\mathbf{z}_k$  refers to the object’s orientation with respect to the camera coordinate,  $\mathbf{R}_{co,k}$ , obtained in Section 3.3.1. The measurement model is a function of the camera pose (orientation part),  $\mathbf{R}_{wc,k}$ , and the object’s orientation,  $\mathbf{R}_{wo}$ , in the world frame:

$$h(\mathbf{R}_{wo}, \mathbf{R}_{wc,k}) = \mathbf{R}_{wc,k}^{-1} \mathbf{R}_{wo}. \quad (11)$$

We formulate the optimization problem by creating the residual between the object orientation,  $\mathbf{R}_{wo}$ , and the per-frame measurement,  $\mathbf{R}_{co,k}$ :

$$\mathbf{r}_k(\mathbf{R}_{wo}) = \log \left( \mathbf{R}_{co,k} h(\mathbf{R}_{wo}, \mathbf{R}_{wc,k})^{-1} \right)^\vee, \quad (12)$$

where  $\mathbf{r}_k(\mathbf{R}_{wo})$  is expressed in Lie algebra  $\mathfrak{so}(3)$ . To account for rotational symmetries, we explicitly consider them alongside the measurement  $\mathbf{R}_{co,k}$  in Equation 12. Generally, when an object has symmetry, there exists a set of orientations that leave the object’s appearance unchanged:

$$\mathbf{S}(\mathbf{R}_{co}) = \left\{ \mathbf{R}'_{co} \in \mathbb{SO}(3) \text{ s.t. } \forall \mathcal{G}(\mathbf{R}_{co}) = \mathcal{G}(\mathbf{R}'_{co}) \right\}, \quad (13)$$

where  $\mathcal{G}(\mathbf{R}_{co})$  is the rendered image of the object under orientation  $\mathbf{R}_{co}$  (assuming the same object translation). We can update the measurement  $\mathbf{R}_{co,k}$  in Equation 12 to  $\bar{\mathbf{R}}_{co,k}$ :

$$\bar{\mathbf{R}}_{co,k} = \operatorname{argmin}_{\mathbf{R}'_{co,k} \in \mathbf{S}(\mathbf{R}_{co,k})} \left\| \log \left( (\mathbf{R}'_{co,k}) h(\mathbf{R}_{wo}, \mathbf{R}_{wc,k})^{-1} \right)^\vee \right\|, \quad (14)$$

where  $\|\cdot\|$  denotes the absolute angle of a 3D rotation vector  $\phi$ , and  $\bar{\mathbf{R}}_{co,k}$  is the updated orientation measurement that has the minimal loss relative to  $\mathbf{R}_{wo}$ .

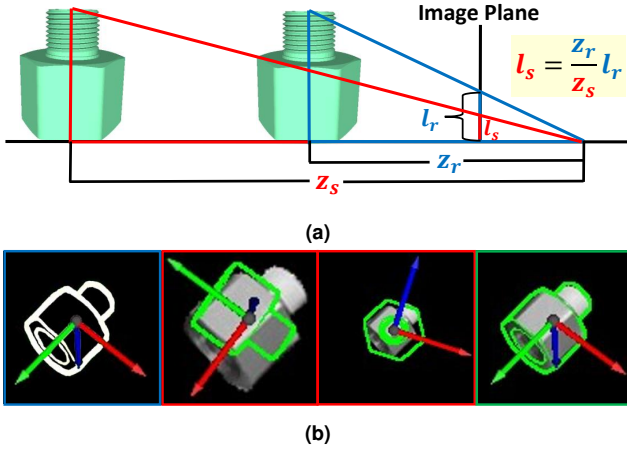


**Figure 5.** (a). The inference of object size  $l_s$  from its projective ratio. (b) Left: the rendered object template at a canonical distance. Middle: incorrect object orientation estimates due to the scale change. Right: re-cropped object ROI using the object translation estimate, leading to the correct result.

### 3.3.3 Measurement ambiguities

Due to the complex uncertainties, such unimodal estimates are insufficient to fully capture the uncertainty associated with the object orientation. To this end, we now consider the sum-mixture of Gaussians as the likelihood function:

$$p(\bar{\mathbf{z}}_k | \mathbf{X}) = \sum_{i=1}^N w_i \mathcal{N}(\boldsymbol{\mu}_i, \boldsymbol{\Sigma}_i), \quad (15)$$

where  $\bar{\mathbf{z}}_k$  is the updated measurement (using Equation 14), and each  $\mathcal{N}(\boldsymbol{\mu}_i, \boldsymbol{\Sigma}_i)$  represents a distinct Gaussian distribution, with  $w_i$  being the weight for component  $i$ . A challenge with the sum-mixture model is that the MLE solution becomes more complex and falls outside the support of common NLLS optimization approaches. To address this, we consider the max-marginal and solve the optimization problem using the following max-mixture formulation (Olson and Agarwal 2013):

$$p(\bar{\mathbf{z}}_k | \mathbf{X}) = \max_{i=1:N} w_i \mathcal{N}(\boldsymbol{\mu}_i, \boldsymbol{\Sigma}_i). \quad (16)$$

The max operator acts as a selector, reducing the problem to a common NLLS optimization. It's important to note that the max-mixture does not make a permanent selection. During each iteration of the optimization, only one of the Gaussian components is selected and optimized. Specifically, given a new orientation measurement  $\bar{\mathbf{R}}_{co,k}$  at frame  $k$ , we actually evaluate each Gaussian component in Equation 16 by computing the absolute orientation angle error,  $\theta_{k,i}$ , between  $\bar{\mathbf{R}}_{co,k}$  and  $h(\mathbf{R}_{wo,i}, \mathbf{R}_{wc,k})$ ,

$$\theta_{k,i} = \left\| \log \left( \bar{\mathbf{R}}_{co,k} h(\mathbf{R}_{wo,i}, \mathbf{R}_{wc,k})^{-1} \right)^\vee \right\|, \quad (17)$$

and select the component with the minimal angle error. To reduce the impact of outliers, the selected Gaussian component will only accept an orientation measurement if the orientation angle error  $\theta_{k,i}$  is below a pre-defined threshold ( $30^\circ$  in our implementation). If the measurement  $\bar{\mathbf{R}}_{co,k}$  is not accepted by any Gaussian component, it will

be treated as a new component and added to the current Gaussian-mixture model.

For each Gaussian component, we optimize the object orientation  $\mathbf{R}_{wo}$  by constructing the following residual  $\mathbf{r}(\mathbf{R}_{wo})$  at frame  $k$ :

$$\mathbf{r}_k(\mathbf{R}_{wo}) = \log \left( \bar{\mathbf{R}}_{co,k}^{-1} \mathbf{R}_{wc,k}^{-1} \mathbf{R}_{wo} \right)^\vee. \quad (18)$$

We perform the optimization in the tangent space  $\mathfrak{so}(3)$ . Following the standard Lie algebra derivation method, we apply a left disturbance  $\Delta\phi$  to  $\mathbf{R}_{wo}$ , and the residual error becomes:

$$\hat{\mathbf{r}}_k = \ln \left( \bar{\mathbf{R}}_{co,k}^{-1} \mathbf{R}_{wc,k}^{-1} \exp(\Delta\phi)^\wedge \mathbf{R}_{wo} \right)^\vee \quad (19)$$

$$= \ln \left( \bar{\mathbf{R}}_{co,k}^{-1} \mathbf{R}_{wc,k}^{-1} \mathbf{R}_{wo} \exp(\mathbf{R}_{wo}^{-1} \Delta\phi)^\wedge \right)^\vee \quad (20)$$

$$\approx \ln \left( \bar{\mathbf{R}}_{co,k}^{-1} \mathbf{R}_{wc,k}^{-1} \mathbf{R}_{wo} \left( 1 + (\mathbf{R}_{wo}^{-1} \Delta\phi)^\wedge \right) \right)^\vee \quad (21)$$

$$= \ln \left( \exp(\mathbf{r}_k)^\wedge + \bar{\mathbf{R}}_{co,k}^{-1} \mathbf{R}_{wc,k}^{-1} \mathbf{R}_{wo} (\mathbf{R}_{wo}^{-1} \Delta\phi)^\wedge \right)^\vee \quad (22)$$

$$= \mathbf{r}_k + \ln \left( \exp(\mathbf{r}_k)^\wedge \exp(\mathbf{R}_{wo}^{-1} \Delta\phi)^\wedge \right) \quad (23)$$

$$= \mathbf{r}_k + \frac{\partial \mathbf{r}_k}{\partial \Delta\phi} \Delta\phi \quad (24)$$

$$= \mathbf{r}_k + \mathbf{J}_{\phi_{wo,k}} \Delta\phi, \quad (25)$$

where

$$\mathbf{J}_{\phi_{wo,k}} = \mathbf{J}_r^{-1}(\mathbf{r}_k) (\mathbf{R}_{wo}^{-1}) \quad (26)$$

$$\approx \mathbf{I}(\mathbf{r}_k) (\mathbf{R}_{wo}^{-1}), \quad (27)$$

where  $\mathbf{J}_r$  is the right Jacobian of  $\mathbb{S}\mathbb{O}(3)$ , which can be approximated as the identity matrix when the errors are small. The final Jacobian,  $\mathbf{J}_{\phi_{wo,k}}$ , for each orientation measurement is a  $3 \times 3$  matrix.

Similar to the 3D translation approach (Equation 6), we optimize the object orientation,  $\mathbf{R}_{wo}$ , using the Gauss-Newton solver:

$$\left( \mathbf{J}_{\phi_{wo}}^T \boldsymbol{\Lambda}_\phi \mathbf{J}_{\phi_{wo}} \right) \delta\phi_{wo} = \mathbf{J}_{\phi_{wo}}^T \boldsymbol{\Lambda}_\phi \mathbf{r}(\mathbf{R}_{wo}), \quad (28)$$

where  $\mathbf{r}(\mathbf{R}_{wo})$  is the stacked rotation residual vector across multiple viewpoints. The stacked Jacobian matrix,  $\mathbf{J}_{\phi_{wo}}$ , and the stacked measurement weight matrix,  $\boldsymbol{\Lambda}_\phi$ , are given by:

$$\mathbf{J}_{\phi_{wo}} = \begin{bmatrix} \mathbf{J}_{\phi_{wo,1}} \\ \vdots \\ \mathbf{J}_{\phi_{wo,K}} \end{bmatrix}, \quad \boldsymbol{\Lambda}_\phi = \begin{bmatrix} \boldsymbol{\Lambda}_{\phi,1} & & \\ & \ddots & \\ & & \boldsymbol{\Lambda}_{\phi,K} \end{bmatrix} \quad (29)$$

The row-blocks,  $\mathbf{J}_{\phi_{wo,k}}$ , and  $\boldsymbol{\Lambda}_{\phi,k}$  correspond to the Jacobian matrix and the measurement covariance matrix for the  $k^{\text{th}}$  viewpoint. The per-frame Jacobian matrix is obtained from Equation 26. For the weight matrix  $\boldsymbol{\Lambda}_{\phi,k}$ , we approximate it by placing the LINE-2D confidence score on its diagonal elements.

To compute the weight,  $w_i$ , for each Gaussian component, we accumulate the LINE-2D confidence score,  $c_i$ , from the orientation measurements within each component across the viewpoints. The weight can be approximated as:

$$w_i = \frac{c_i}{\sum_i c_i}. \quad (30)$$

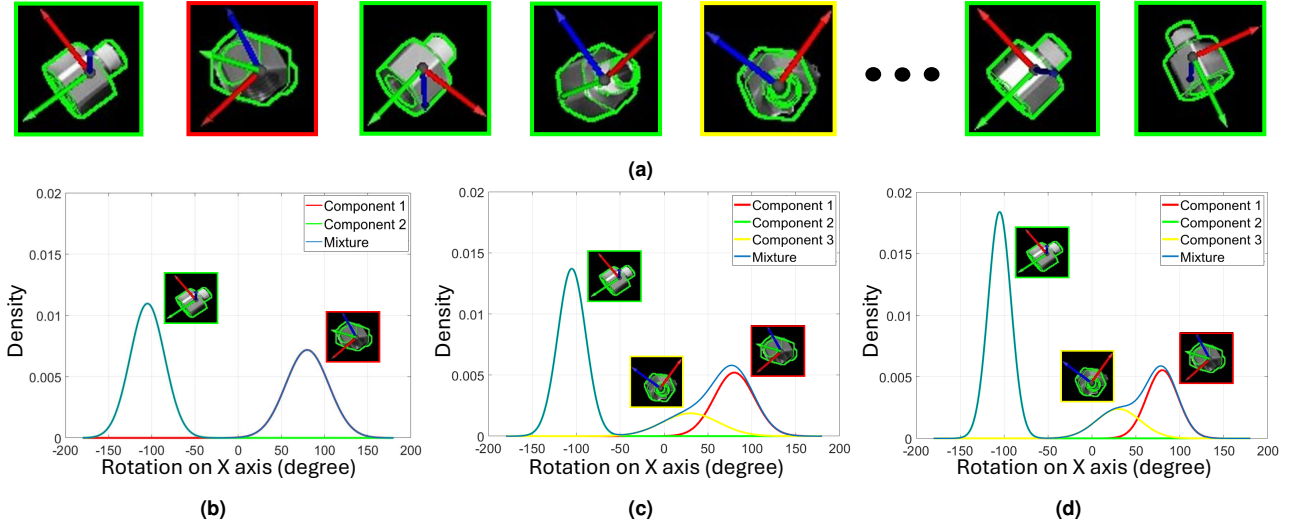


**Figure 6.** Max-mixtures for processing the object orientation measurements. Note that we show the distribution only on one axis for demonstration purposes. (a) Acquired orientation measurements from different viewpoints. (b) Mixture distribution after two viewpoints. (c) Mixture distribution after five viewpoints. (d) Mixture distribution after eight viewpoints.

This processing is illustrated in Figure 6. Given the measurements from two viewpoints, the object orientation distribution  $P(\mathbf{R}_{wo})$  is represented with two Gaussian components (green and red) with similar weights. When additional viewpoints are incorporated, a third component (yellow) is added. As more orientation measurements are received (i.e. after five viewpoints), the weight of the correct component (green) increases, surpassing the other hypotheses.

## 4 Active Pose Estimation using Next-Best-View

In Section 3.1, we solve the multi-view object pose estimation problem using a two-step optimization formulation. However, the accuracy of the estimated object pose heavily depends on the collected RGB measurements from the selected camera viewpoints. Moreover, in many real-world applications, capturing a large number of viewpoints is impractical. To overcome this limitation, we introduce an active object pose estimation process. This approach not only estimates the uncertainty of the object pose but also predicts the next-best-view to minimize that uncertainty.

### 4.1 Initialization and Uncertainty Estimation

We initialize our active object pose estimation process with a collection of measurement sets,  $\mathbf{Z}_{1:K}$ , from  $K$  camera viewpoints and perform iterative optimization to estimate the object's 6D pose. To bootstrap the system, at least  $K = 2$  viewpoints are required. As described in Section 3.1, we decompose the full 6D object pose into 3D translation,  $\mathbf{t}_{wo}$ , and 3D orientation,  $\mathbf{R}_{wo}$ . As a result, we compute their uncertainties independently.

#### 4.1.1 3D Translation

As discussed in Section 3.2, we assume that the object's translation,  $\mathbf{t}_{wo}$ , follows a unimodal Gaussian distribution,  $\mathcal{N}(\mathbf{t}_{wo}|\mu, \Sigma)$ . The translation is estimated via Equation 6,

using the stacked Jacobian,  $\mathbf{J}_{\mathbf{t}_{wo}, \mathbf{u}_{1:K}}$ , and the stacked measurement uncertainties,  $\Sigma_{\mathbf{u}_{1:K}}$ :

$$\mathbf{J}_{\mathbf{t}_{wo}, \mathbf{u}_{1:K}} = \begin{bmatrix} \mathbf{J}_{\mathbf{t}_{wo}, \mathbf{u}_1} \\ \vdots \\ \mathbf{J}_{\mathbf{t}_{wo}, \mathbf{u}_K} \end{bmatrix}, \Sigma_{\mathbf{u}_{1:K}} = \begin{bmatrix} \Sigma_{\mathbf{u}_1} & & \\ & \ddots & \\ & & \Sigma_{\mathbf{u}_K} \end{bmatrix}, \quad (31)$$

where  $\mathbf{u}_{1:K}$  denotes the object 2D center measurements from  $K$  camera viewpoints. As illustrated in Figure 7a, we compute the covariance of the object translation,  $\Sigma_{\mathbf{t}_{wo}, \mathbf{u}_{1:K}}$ , through a first-order approximation of the Fisher information matrix (FIM):

$$\Sigma_{\mathbf{t}_{wo}, \mathbf{u}_{1:K}} = (\mathbf{J}_{\mathbf{t}_{wo}, \mathbf{u}_{1:K}}^T \Sigma_{\mathbf{u}_{1:K}}^{-1} \mathbf{J}_{\mathbf{t}_{wo}, \mathbf{u}_{1:K}})^{-1}. \quad (32)$$

To obtain the entropy from the translation covariance matrix, we employ the differential entropy,  $h_e(\Sigma_{\mathbf{t}_{wo}, \mathbf{u}_{1:K}})$ :

$$h_{\mathbf{t}_{wo}} = h_e(\Sigma_{\mathbf{t}_{wo}, \mathbf{u}_{1:K}}) = \frac{1}{2} \ln \left( (2\pi e)^3 |\Sigma_{\mathbf{t}_{wo}, \mathbf{u}_{1:K}}| \right), \quad (33)$$

where  $h_{\mathbf{t}_{wo}}$  is expressed in nats.

#### 4.1.2 3D Orientation

In contrast, the uncertainty calculation for the object orientation is more complex due to the Gaussian mixture formulation,  $\sum_{i=1}^N w_i \mathcal{N}(\phi_{wo}|\mu_i, \Sigma_i)$ , as shown in Equation 2. While many approaches estimate entropy using sampling methods (Shi et al. 2021), which can be computationally expensive, we instead follow the approach from (Eidenberger and Scharinger 2010) and estimate the orientation entropy using an upper bound approximation for the Gaussian mixture distribution (Huber et al. 2008):

$$h_{\phi_{wo}} \leq h_{\phi_{wo}}^u = \sum_{i=1}^N w_i \left[ -\ln w_i + \frac{1}{2} \ln \left( (2\pi e)^3 |\Sigma_i| \right) \right], \quad (34)$$



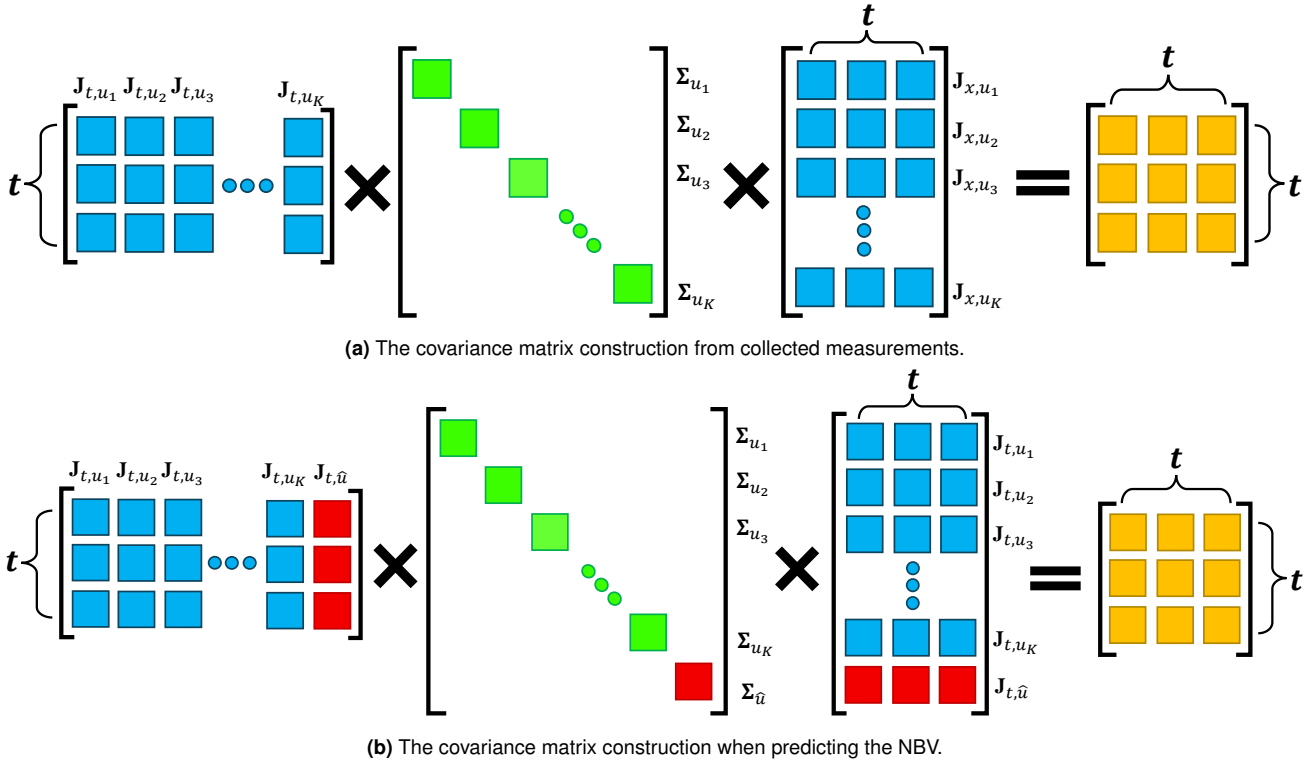


**Figure 7.** Visualization of the covariance matrix construction for object 3D translation. (a) The construction from collected measurements. (b) The construction when predicting NBV.

where  $h_{\phi_{wo}}$  is the true entropy of the Gaussian mixture, and  $h_{\phi_{wo}}^u$  is the upper bound approximation. To estimate the entropy for each individual Gaussian covariance,  $\Sigma_i$ , we re-project the 3D edge points (from model templates) into the image space and evaluate the alignment quality between the projected points and the 2D edge maps from different camera viewpoints. As shown in Figure 8, the orientation uncertainty is low when the re-projected edge points align well with the 2D edge map, and high when the alignment is poor.

We begin by deriving the Jacobian of the projected edge points and their associated measurement uncertainties, which will later be used to compute the orientation covariance. For a set of 3D model edge points,  $\mathbf{o}_k$ , we transform them into the  $k^{\text{th}}$  camera viewpoint and obtain the corresponding projected 2D edge pixels,  $\mathbf{m}_k$ , through re-projection. The

Jacobian,  $\mathbf{J}_{\phi_{wo}, \mathbf{m}_k}$ , is then expressed as:

$$\mathbf{J}_{\phi_{wo}, \mathbf{m}_k} = \frac{\partial \mathbf{m}_k}{\partial \phi_{wo}} = \frac{\partial \mathbf{m}_k}{\partial \mathbf{p}_{c,k}} \frac{\partial \mathbf{p}_{c,k}}{\partial \mathbf{p}_w} \frac{\partial \mathbf{p}_w}{\partial \phi_{wo}}, \quad (35)$$

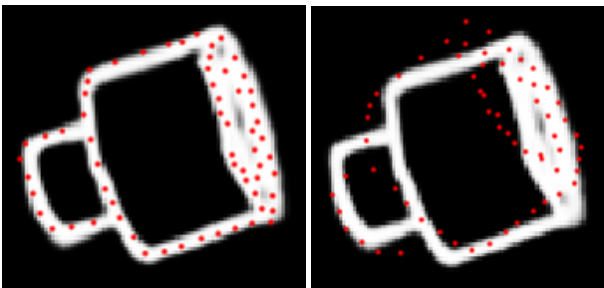
where  $\mathbf{p}_{c,k}$  and  $\mathbf{p}_w$  represent the object’s 3D edge points in the  $k^{\text{th}}$  camera frame and the world frame, respectively. The Jacobian,  $\mathbf{J}_{\phi_{wo}, \mathbf{m}_k}$ , has dimensions  $2N \times 3$ , where  $N$  is the number of 3D object edge points. Note that the Jacobian,  $\mathbf{J}_{\phi_{wo}, \mathbf{m}_k}$ , is distinct from the Jacobian,  $\mathbf{J}_{\phi_{wo}, k}$ , in Equation 26. For the associated measurement uncertainties,  $\Sigma_{\mathbf{m}_k}$ , we approximate them with the inverse of the edge map intensity, placing the values along the diagonal elements and its dimension is  $2N \times 2N$ . The stacked Jacobian,  $\mathbf{J}_{\phi_{wo}, \mathbf{m}_{1:K}}$ , and stacked measurement uncertainties,  $\Sigma_{\mathbf{m}_{1:K}}$ , are given by:

$$\mathbf{J}_{\phi_{wo}, \mathbf{m}_{1:K}} = \begin{bmatrix} \mathbf{J}_{\phi_{wo}, \mathbf{m}_1} \\ \vdots \\ \mathbf{J}_{\phi_{wo}, \mathbf{m}_K} \end{bmatrix}, \Sigma_{\mathbf{m}_{1:K}} = \begin{bmatrix} \Sigma_{\mathbf{m}_1} & & \\ & \ddots & \\ & & \Sigma_{\mathbf{m}_K} \end{bmatrix}. \quad (36)$$

The covariance matrix,  $\Sigma_{\phi_{wo}, \mathbf{m}_{1:K}}$  is finally computed using the Fisher information approximation:

$$\Sigma_{\phi_{wo}, \mathbf{m}_{1:K}} = \left( \mathbf{J}_{\phi_{wo}, \mathbf{m}_{1:K}}^T \Sigma_{\mathbf{m}_{1:K}}^{-1} \mathbf{J}_{\phi_{wo}, \mathbf{m}_{1:K}} \right)^{-1}. \quad (37)$$

To compute the total entropy over the Gaussian mixture, we apply Equations 35-37 to each Gaussian component and



(a) Accurate edge alignment (b) Inaccurate edge alignment.

**Figure 8.** (a) Low orientation uncertainty when edge alignment is accurate ( $h_{\phi_{wo}} = 3.21$  nats). (b) High orientation uncertainty when edge alignment is not accurate ( $h_{\phi_{wo}} = 3.73$  nats).

substitute the results into Equation 34:

$$\begin{aligned} h_{\phi_{w_o}}^u &= \sum_{i=1}^N w_i \left[ -\ln w_i + h_e \left( \Sigma_{\phi_{w_o}, \mathbf{m}_{1:K}, i} \right) \right] \\ &= \sum_{i=1}^N w_i \left[ -\ln w_i + \frac{1}{2} \ln \left( (2\pi e)^3 \left| \Sigma_{\phi_{w_o}, \mathbf{m}_{1:K}, i} \right| \right) \right]. \end{aligned} \quad (38)$$

The final entropy of the 6D object pose is given by:

$$h_{6D} = g_t h_{\mathbf{t}_{w_o}} + g_\phi h_{\phi_{w_o}}^u, \quad (40)$$

where  $g_t$  and  $g_\phi$  are the weights assigned to the translation and orientation entropies, respectively.

## 4.2 Next-Best-View Prediction

To improve object pose accuracy, we aim to find the next best camera viewpoint  $\mathbf{v}^* \sim \mathcal{V}$  that minimize the entropy of the object pose. Here,  $\mathcal{V}$  denotes the set of all potential candidate viewpoints. Suppose we have already collected object center measurements,  $\mathbf{u}_{1:K}$ , and edge measurements,  $\mathbf{m}_{1:K}$ , from  $K$  different camera viewpoints. For a future camera viewpoint,  $\hat{\mathbf{v}}$ , the stacked Jacobian,  $\mathbf{J}_{\mathbf{t}_{w_o}, \bar{\mathbf{u}}}$ , and the stacked measurement uncertainties,  $\Sigma_{\mathbf{t}_{w_o}, \bar{\mathbf{u}}}$ , of the object translation are expressed as follows:

$$\mathbf{J}_{\mathbf{t}_{w_o}, \bar{\mathbf{u}}} = \begin{bmatrix} \mathbf{J}_{\mathbf{t}_{w_o}, \mathbf{u}_{1:K}} \\ \mathbf{J}_{\mathbf{t}_{w_o}, \hat{\mathbf{u}}} \end{bmatrix}, \quad \Sigma_{\mathbf{t}_{w_o}, \bar{\mathbf{u}}} = \begin{bmatrix} \Sigma_{\mathbf{t}_{w_o}, \mathbf{u}_{1:K}} & \mathbf{0} \\ \mathbf{0} & \Sigma_{\mathbf{t}_{w_o}, \hat{\mathbf{u}}} \end{bmatrix}, \quad (41)$$

where  $\bar{\mathbf{u}} = \{\mathbf{u}_{1:K}, \hat{\mathbf{u}}\}$  includes the set of acquired object center measurements  $\mathbf{u}_{1:K}$  from viewpoints  $\mathbf{v}_{1:K}$  and the predicted measurement  $\hat{\mathbf{u}}$  for the future viewpoint,  $\hat{\mathbf{v}}$ .

For the orientation component, similarly, for each Gaussian component, we define the stacked Jacobian,  $\mathbf{J}_{\phi_{w_o}, \bar{\mathbf{m}}}$ , and the associated measurement uncertainties,  $\Sigma_{\phi_{w_o}, \bar{\mathbf{m}}}$ , for the future viewpoint as follows:

$$\mathbf{J}_{\phi_{w_o}, \bar{\mathbf{m}}} = \begin{bmatrix} \mathbf{J}_{\phi_{w_o}, \mathbf{m}_{1:K}} \\ \mathbf{J}_{\phi_{w_o}, \hat{\mathbf{m}}} \end{bmatrix}, \quad \Sigma_{\phi_{w_o}, \bar{\mathbf{m}}} = \begin{bmatrix} \Sigma_{\phi_{w_o}, \mathbf{m}_{1:K}} & \mathbf{0} \\ \mathbf{0} & \Sigma_{\phi_{w_o}, \hat{\mathbf{m}}} \end{bmatrix} \quad (42)$$

Using the Fisher information, we can predict the covariance of the object translation and orientation as:

$$\Sigma_{\mathbf{t}_{w_o}, \bar{\mathbf{u}}} = \left( \mathbf{J}_{\mathbf{t}_{w_o}, \bar{\mathbf{u}}}^T \Sigma_{\mathbf{t}_{w_o}, \bar{\mathbf{u}}}^{-1} \mathbf{J}_{\mathbf{t}_{w_o}, \bar{\mathbf{u}}} \right)^{-1}, \quad (43)$$

$$\Sigma_{\phi_{w_o}, \bar{\mathbf{m}}} = \left( \mathbf{J}_{\phi_{w_o}, \bar{\mathbf{m}}}^T \Sigma_{\phi_{w_o}, \bar{\mathbf{m}}}^{-1} \mathbf{J}_{\phi_{w_o}, \bar{\mathbf{m}}} \right)^{-1}. \quad (44)$$

We illustrate this process for the translation component in Figure 7b. Note that, in Equations (41) and (42), we compute the Jacobians,  $\mathbf{J}_{\mathbf{t}_{w_o}, \hat{\mathbf{u}}}$ ,  $\mathbf{J}_{\phi_{w_o}, \hat{\mathbf{m}}}$ , and measurement uncertainties,  $\Sigma_{\mathbf{t}_{w_o}, \hat{\mathbf{u}}}$ ,  $\Sigma_{\phi_{w_o}, \hat{\mathbf{m}}}$ , prior to actually moving to the future camera viewpoint  $\hat{\mathbf{v}}$ . These Jacobians are computed based on the object pose estimate derived from the measurements  $\mathbf{u}_{1:K}$  and  $\mathbf{m}_{1:K}$ . For measurement uncertainties, we assume that they remain constant across different future viewpoints.

We determine our NBV from the candidate viewpoint set,  $\mathcal{V}$ , by minimizing the weighted sum of the translation and

orientation entropy:

$$\begin{aligned} \mathbf{v}^* &= \underset{\hat{\mathbf{v}}}{\operatorname{argmin}} g_t h_e \left( \Sigma_{\mathbf{t}_{w_o}, \bar{\mathbf{u}}} \right) \\ &\quad + g_\phi \sum_{i=1}^N w_i \left[ -\ln w_i + h_e \left( \Sigma_{\phi_{w_o}, \bar{\mathbf{m}}, i} \right) \right], \end{aligned} \quad (45)$$

where  $g_t$  and  $g_\phi$  are the entropy weights for the translation and orientation components, respectively. Once the next-best-view  $\mathbf{v}^*$  is determined, the camera is moved, and new measurements,  $\mathbf{u}^*$ ,  $\mathbf{m}^*$ , are collected from the corresponding viewpoint. These new measurements are then appended as follows:

$$\mathbf{u}_{1:K} \cup \mathbf{u}^* \rightarrow \mathbf{u}_{1:K+1}, \quad \mathbf{m}_{1:K} \cup \mathbf{m}^* \rightarrow \mathbf{m}_{1:K+1}. \quad (46)$$

The object translation and orientation are then recomputed, and the NBV selection process is repeated using Equations (41)–(45). This iterative process continues until the predicted entropy falls below a user-defined threshold or until a maximum number of viewpoints has been selected.

## 5 Experiments

### 5.1 Datasets

We evaluate our framework on two challenging real-world datasets, the public ROBI dataset (Yang et al. 2021) and a new dataset of textureless transparent objects which we created for this work. The ROBI dataset (Yang et al. 2021) provides multiple camera viewpoints for seven textureless reflective industrial parts. The objects were placed in challenging bin scenarios and recorded from multiple camera viewpoints using two sensors: a high-cost Ensenso camera and a low-cost RealSense camera. As shown in the ROBI dataset, the RealSense camera exhibits significantly lower depth accuracy than the Ensenso camera.

**T-ROBI Dataset.** To further validate the effectiveness of our approach, we introduce the T-ROBI (Transparent Reflective Objects in BIns) dataset. This dataset includes two representative components: a ‘‘Bottle’’ and a ‘‘Pipe Fitting’’, as illustrated in Figure 9. Unlike other publicly available transparent object datasets (Sajjan et al. 2020; Liu et al. 2020; Xu et al. 2021), which typically focus on isolated objects, our dataset presents a more challenging scenario. It consists of images containing multiple identical parts randomly stacked within a bin, thereby significantly increasing the difficulty of object pose estimation. For each object, we captured 6 distinct scenes from 55 camera viewpoints using the high-cost Ensenso N35 camera (IDS 2025). For each viewpoint, both monochrome images and depth maps are provided. However, as illustrated in Figure 9b, the transparency of the objects results in significant depth inaccuracies or missing data, making it particularly challenging to label ground truth 6D object poses. To address this, we adopted the ground truth labeling method from the ROBI dataset (Yang et al. 2021), utilizing a scanning spray (AESUB 2025) to capture accurate ground truth depth maps of all bins. The example ground truth depth map, object CAD model, and annotated 6D object poses of the T-ROBI dataset are shown in Figures 9c, 9d, and 9e, respectively. Upon the publication of this work, we will release a public version of our T-ROBI dataset.

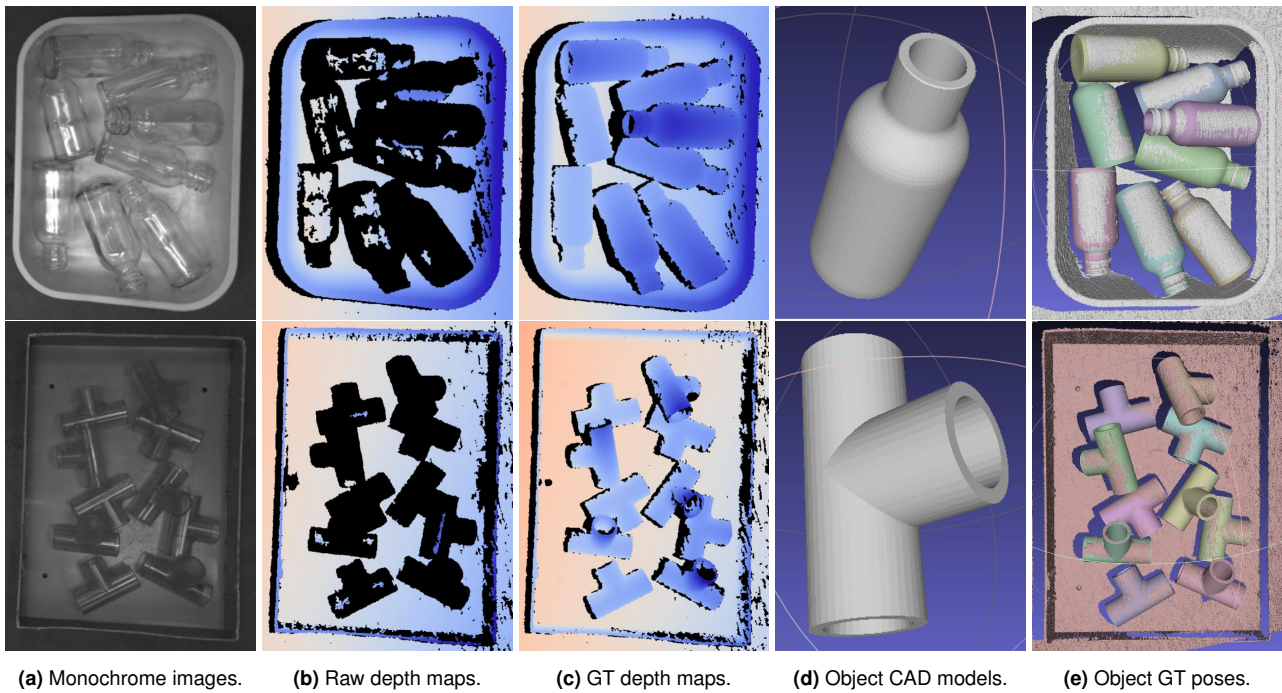


**Figure 9.** T-ROBI dataset: (upper) the object "Bottle" and (lower) the object "Pipe Fitting." (a) Monochrome images. (b) Raw depth maps. (c) Ground truth depth maps. (d) 3D CAD models of the objects. (e) Ground truth 6D object poses.

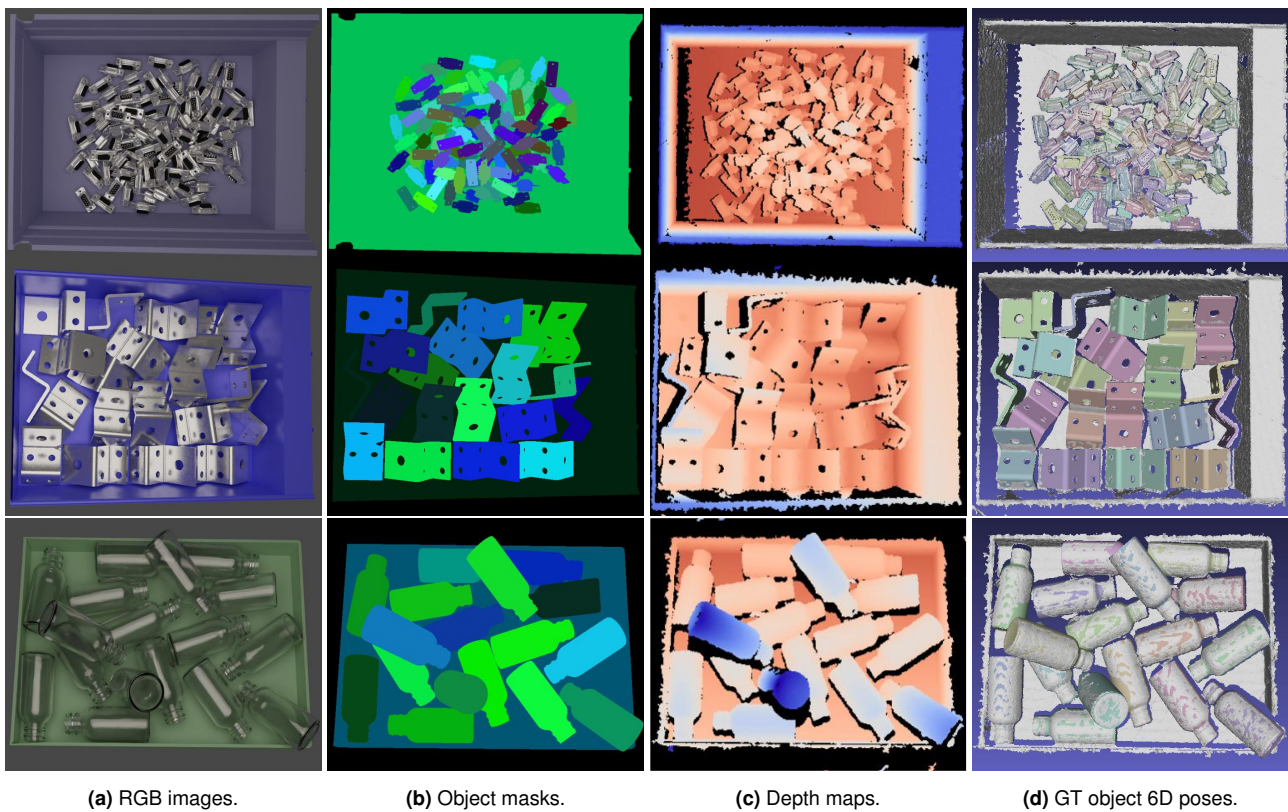


**Figure 10.** Examples of our generated **synthetic data** using the Blender rendering software (Community 2018) with the Bullet physics engine (Coumans and Bai 2016). (a) The RGB images. (b) The object masks. (c) The depth maps. (d) The ground truth 6D object poses. From top to bottom: the object "D-Sub Connector", "Zigzag" from ROBI dataset (Yang et al. 2021) and "Bottle" from T-ROBI dataset.

This dataset is designed to support 6D pose estimation (Liu et al. 2020; Chen et al. 2023) as well as depth estimation tasks (Sajjan et al. 2020; Xu et al. 2021) for transparent

objects in challenging cluttered and occluded bin-picking scenes.

**Synthetic Dataset.** To facilitate network training, we created a large-scale synthetic dataset comprising objects

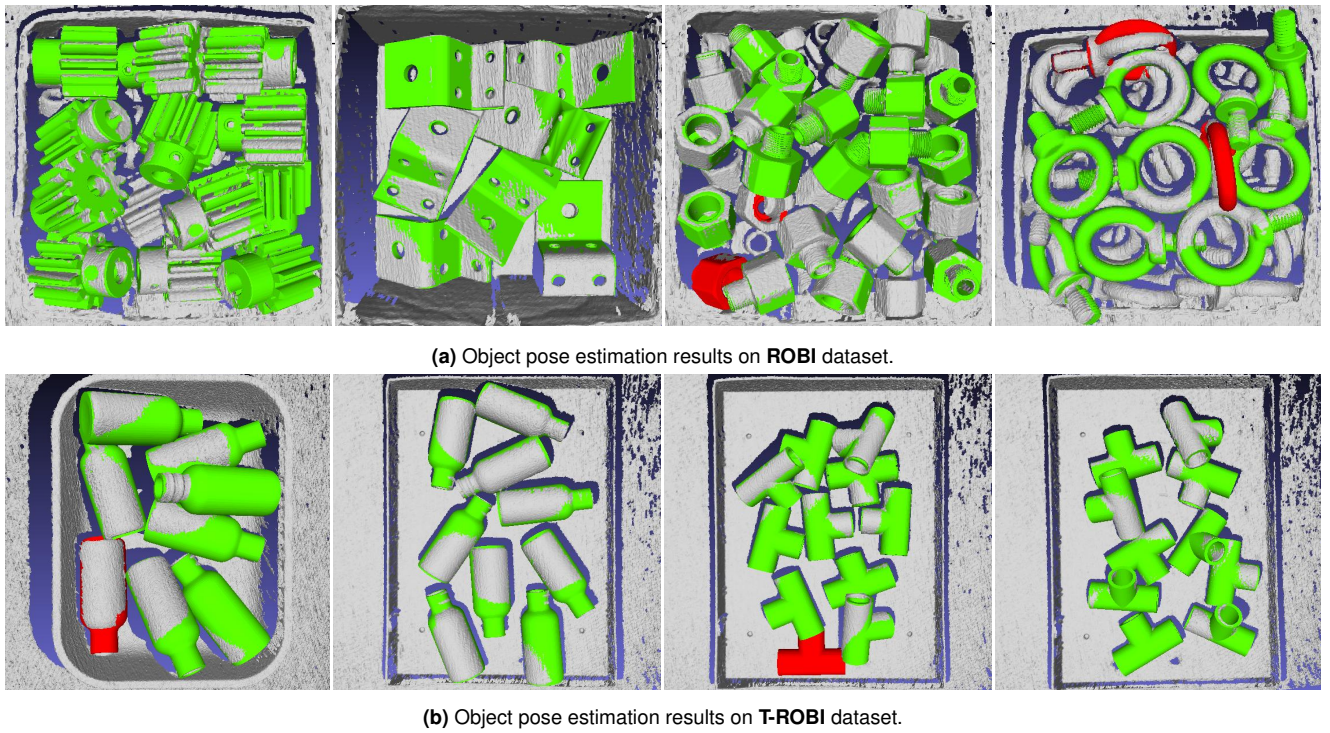


**Figure 11.** Qualitative results of our approach for the **ROBI** and **T-ROBI** datasets. Pose estimation performance is depicted using color coding: green indicates detections that satisfy the ADD metric, while red indicates those that do not. The results are generated using 8 camera viewpoints. To enhance visualization, the estimated object poses are overlaid on the ground truth depth map. (a) Results on the ROBI dataset. (b) Results on the T-ROBI dataset.

from both the ROBI and T-ROBI datasets, as illustrated in Figure 10. For each scene, we provide the RGB images, depth maps, object masks, and 6D poses. Our simulation environment is built using the Bullet physics engine (Coumans and Bai 2016) in conjunction with Blender software (Community 2018). The process begins with importing each object’s CAD model into Blender, where we manually specify its color and material properties. After preparing the object, we load it into the simulation and drop it from various positions and orientations within the bin using the Bullet physics engine. This approach allows us to generate a wide variety of object poses, clutter levels, and occlusions. Next, we adjust both the light source and camera pose to different viewpoints above the bin and render the scene using Blender, resulting in high-quality visual representations for our dataset. Finally, we utilize the Ensenso SDK (IDS 2025) to generate synthetic depth images, as shown in Figure 10c. For each object, we produce approximately 6,000 to 13,000 images. We will also release our synthetic dataset upon publication.

## 5.2 Baselines, Implementations and Evaluation Metrics

We quantitatively evaluate our approach against three prominent baselines: Multi-View 3D Keypoints (MV-3D-KP) (Li and Schoellig 2023) and two variants of CosyPose (Labbé et al. 2020). To ensure a fair comparison, all methods are trained only on the synthetic dataset (described in Section 5.1). During runtime, we utilize identical object bounding box detections and provide ground truth multi-view camera poses.

- **MV-3D-KP.** Multi-View 3D Keypoints (MV-3D-KP) (Li and Schoellig 2023) builds upon the single-view approach of PVN3D (He et al. 2020) and specializes in estimating 6D object poses by leveraging both RGB and depth data. MV-3D-KP provides excellent scalability, allowing for the incorporation of additional views that enhance accuracy and reduce uncertainty in pose estimation. As shown in (Li and Schoellig 2023), this method demonstrates exceptional performance on the ROBI dataset, setting a high standard in the field.
- **CosyPose+PVNet.** CosyPose (Labbé et al. 2020) is a multi-view pose fusion solution which takes the 6D object pose estimates from individual viewpoints as the input and optimizes the overall scene consistency. Note that, CosyPose is an offline batch-based solution that is agnostic to any particular pose estimator. In our implementation, we utilize a learning-based approach, Pixel-Wise Voting Network (PVNet) (Peng et al. 2019), to acquire the single view pose estimates. The PVNet approach first detects 2D keypoints and then solves a Perspective-n-Point (PnP) problem for pose estimation. This approach naturally deals with object occlusion and achieves remarkable performance.
- **CosyPose+LINE2D.** To provide single view pose estimates for CosyPose, we additionally utilize the LINE-2D pose estimator. In our implementation, we utilize the LINE-2D pose estimator with the same object center, object edge, and segmentation mask (from our MEC-Net). To feed the reliable single-view estimates to CosyPose, we use two strategies to obtain scale information. For the first strategy, we

Objects		4 Views					8 Views				
		CosyPose +PVNet	CosyPose +LINE2D		MV- 3D-KP	Ours	CosyPose +PVNet	CosyPose +LINE2D		MV- 3D-KP	Ours
Input Modality		RGB	RGB	RGBD	RGBD	RGB	RGB	RGBD	RGBD	RGBD	RGB
Tube Fitting	ADD	39.4	32.5	74.8	<b>94.0</b>	89.4	61.6	50.3	91.4	<b>96.0</b>	94.0
	(5,10)	47.7	45.7	76.2	<b>95.4</b>	88.1	64.9	71.5	94.7	<b>96.0</b>	92.0
Chrome Screw	ADD	17.4	55.7	73.0	<b>90.8</b>	86.7	24.4	70.1	88.5	91.9	<b>93.7</b>
	(5,10)	18.6	63.2	78.2	<b>88.5</b>	85.1	30.8	78.7	90.2	<b>90.8</b>	90.2
Eye Bolt	ADD	21.6	35.1	85.1	<b>93.2</b>	93.2	46.0	79.7	93.2	<b>94.6</b>	94.6
	(5,10)	12.2	27.0	78.4	<b>87.8</b>	67.6	31.1	64.9	83.8	<b>85.1</b>	75.8
Gear*	ADD	50.6	25.9	80.2	85.2	<b>91.4</b>	71.6	43.2	88.9	93.8	<b>97.5</b>
	(5,10)	34.6	29.6	79.0	85.2	<b>85.2</b>	49.4	45.7	92.6	91.4	<b>93.8</b>
Zigzag	ADD	89.7	65.5	87.9	<b>96.6</b>	94.8	89.7	77.6	96.6	96.6	<b>98.3</b>
	(5,10)	82.8	37.9	75.9	<b>93.1</b>	89.7	86.2	63.8	93.1	<b>96.6</b>	93.1
DIN Connector	ADD	13.3	15.6	57.8	<b>90.6</b>	69.5	28.1	24.2	64.1	<b>93.8</b>	73.4
	(5,10)	18.8	12.5	46.1	<b>84.4</b>	53.9	32.0	23.4	51.6	<b>93.0</b>	59.4
D-Sub Connector <sup>†</sup>	ADD	11.2	9.9	55.3	<b>92.5</b>	79.5	18.0	15.5	63.3	<b>95.7</b>	84.5
	(5,10)	11.2	11.2	39.1	<b>83.2</b>	47.2	16.8	11.2	41.6	<b>91.3</b>	55.9
ALL	ADD	34.7	34.3	73.4	<b>91.8</b>	86.4	48.5	51.5	83.7	<b>94.6</b>	90.9
	(5,10)	32.3	32.4	67.6	<b>88.2</b>	73.8	44.5	51.3	78.2	<b>92.0</b>	80.0

\*In our evaluation, we treat the object ‘‘Gear’’ as symmetric about the Z-axis with an order of 12.

<sup>†</sup>In our evaluation, we treat the object ‘‘D-Sub Connector’’ as symmetric about the Z-axis with an order of 2.

**Table 1.** Detection rates of 6D object pose estimation on **Ensenso** test set from **ROBI** dataset, evaluated with the metrics of ADD and ( $5\text{ mm}, 10^\circ$ ). There are a total of nine scenes for each object.

Objects		4 Views					8 Views				
		CosyPose +PVNet	CosyPose +LINE2D		MV- 3D-KP	Ours	CosyPose +PVNet	CosyPose +LINE2D		MV- 3D-KP	Ours
Input Modality		RGB	RGB	RGBD	RGBD	RGB	RGB	RGBD	RGBD	RGBD	RGB
Tube Fitting	ADD	26.7	27.9	70.6	80.9	<b>86.8</b>	47.1	69.1	83.9	82.4	<b>85.3</b>
	(5,10)	36.8	48.5	72.1	67.6	<b>79.4</b>	44.2	82.3	85.3	70.6	<b>91.2</b>
Chrome Screw	ADD	10.0	58.6	68.5	78.6	<b>92.9</b>	30.0	77.1	80.0	84.3	<b>92.9</b>
	(5,10)	10.0	64.3	<b>82.9</b>	80.0	77.1	42.9	85.7	<b>94.3</b>	90.0	87.1
Eye Bolt	ADD	17.7	58.8	76.5	88.2	<b>94.1</b>	38.2	73.5	<b>94.1</b>	85.3	<b>94.1</b>
	(5,10)	17.7	41.2	67.6	<b>79.4</b>	55.9	29.4	61.8	<b>91.2</b>	79.4	76.5
Gear*	ADD	38.9	36.1	83.3	80.6	<b>94.4</b>	44.4	55.6	<b>97.2</b>	88.9	<b>97.2</b>
	(5,10)	27.8	38.9	77.8	52.8	<b>86.1</b>	30.6	58.3	<b>94.4</b>	72.2	88.9
Zigzag	ADD	60.7	42.9	78.6	<b>96.4</b>	89.3	85.7	71.4	92.9	<b>96.4</b>	<b>96.4</b>
	(5,10)	53.6	21.4	71.4	<b>92.9</b>	85.7	82.1	64.3	92.9	<b>96.4</b>	92.9
DIN Connector	ADD	11.5	3.8	36.5	<b>86.5</b>	51.9	15.4	15.4	51.9	<b>84.6</b>	82.7
	(5,10)	13.5	1.9	30.8	<b>76.9</b>	32.7	26.9	9.6	34.6	<b>84.6</b>	57.7
D-Sub Connector <sup>†</sup>	ADD	8.3	6.9	40.3	<b>81.9</b>	70.8	20.8	9.7	45.8	83.3	<b>81.9</b>
	(5,10)	9.7	6.9	18.1	<b>45.8</b>	31.9	18.1	8.3	33.3	43.1	<b>43.1</b>
ALL	ADD	24.8	33.6	64.9	<b>84.7</b>	82.9	40.2	53.1	78.0	86.5	<b>90.1</b>
	(5,10)	24.2	31.9	60.1	<b>70.8</b>	64.1	39.2	52.9	75.1	76.6	<b>76.8</b>

\*In our evaluation, we treat the object ‘‘Gear’’ as symmetric about the Z-axis with an order of 12.

<sup>†</sup>In our evaluation, we treat the object ‘‘D-Sub Connector’’ as symmetric about the Z-axis with an order of 2.

**Table 2.** Detection rates of 6D object pose estimation on **RealSense** test set from **ROBI** dataset, evaluated with the metrics of ADD and ( $5\text{ mm}, 10^\circ$ ). There are a total of four scenes for each object.

generate the templates at multiple distances during training (9 distances in our experiments) and perform standard template matching at inference time. This strategy can significantly improve the single view pose estimation performance by sacrificing run-time speed and is treated as the RGB version. For the second strategy, we directly use the depth images at inference

time to acquire the object scale and refer to it as the RGB-D version.

We implement our MEC-Net using the PyTorch library, employing ResNet-18 (He et al. 2016) as the backbone network. The MEC-Net is trained from scratch using the Adam optimizer (Kingma and Ba 2015), with a batch size of

Objects		4 Views					8 Views				
		CosyPose +PVNet	CosyPose +LINE2D		MV- 3D-KP	Ours	CosyPose +PVNet	CosyPose +LINE2D		MV- 3D-KP	Ours
Input Modality		RGB	RGB	RGBD	RGBD	RGB	RGB	RGB	RGBD	RGBD	RGB
Bottle	ADD	32.7	38.5	1.9	3.8	<b>90.4</b>	48.1	53.8	3.8	1.9	<b>90.4</b>
	(5,10)	17.3	13.5	1.9	3.8	<b>73.1</b>	28.9	38.5	3.8	1.9	<b>75.0</b>
Pipe Fitting	ADD	30.4	51.8	28.6	67.9	<b>96.4</b>	39.3	71.4	37.5	64.3	<b>100.0</b>
	(5,10)	14.3	35.7	12.5	60.7	<b>85.7</b>	28.6	41.7	17.9	62.5	<b>87.5</b>
ALL	ADD	31.0	45.2	15.3	35.9	<b>93.4</b>	45.6	62.6	20.7	33.1	<b>95.2</b>
	(5,10)	15.8	24.6	7.2	32.3	<b>79.4</b>	26.8	40.1	10.9	32.2	<b>81.3</b>

**Table 3.** Detection rates of 6D object pose estimation on **T-ROBI** dataset, evaluated with the metrics of ADD and  $(5\text{ mm}, 10^\circ)$ . There are a total of six scenes for each object.

640 and a learning rate of 0.01 over 100 epochs on an RTX A6000 GPU. To ensure a fair comparison between MV-3D-KP and PVNet, we use the same ResNet-18 backbone and maintain consistent hyperparameters during training.

We adopt two metrics to evaluate pose estimation performance. The first metric is the average distance (ADD) metric (Hinterstoisser et al. 2012). We transform the object model points by the ground truth and the estimated 6D poses, respectively, and compute the mean of the pairwise distances between the two transformed point sets. A pose is claimed as correct if its ADD is smaller than 10% of the object diameter. However, as demonstrated in (Yang et al. 2024), the ADD metric is not strict enough and can tolerate up to 30-degree orientation error on some objects. Hence, we additionally use the 5-mm/10-degree  $(5\text{ mm}, 10^\circ)$  metric, which is more strict on orientation error. It considers an object pose as correct if the translation error is smaller than 5 mm and the orientation error is smaller than 10 degrees. In our evaluation, we consider a ground truth pose only if its visibility score is larger than 75%.

### 5.3 Results on ROBI Dataset

We conduct the experiments on the ROBI dataset with a variable number of viewpoints (4 and 8). The object pose estimation results are presented in Table 1 and 2 for Ensenso and RealSense test set, respectively. The results show our method outperforms the RGB baseline by a wide margin, and is competitive with the RGB-D approaches, without the need for depth measurements.

In the Ensenso test set, it is noteworthy that “MV-3D-KP” demonstrates exceptional performance, achieving state-of-the-art results on the ROBI dataset. This success is largely attributed to the high-quality depth maps produced by the Ensenso 3D camera. Specifically, when utilizing RGB-D data, the “MV-3D-KP” method achieves an overall detection rate of 91.8% using four views and 94.6% using eight views, as measured by the ADD metric. Additionally, it achieves an overall detection rate of 88.2% with four views and 92.0% with eight views using the  $(5\text{ mm}, 10^\circ)$  metric. In comparison, despite relying solely on RGB data, our approach demonstrates competitive performance, with detection rates only 5.4% and 3.7% lower than MV-3D-KP for four-view and eight-view data, respectively, as measured by the ADD metric. When utilizing only RGB images, our approach significantly outperforms both

“CosyPose+PVNet” and “CosyPose+LINE2D,” achieving margins of at least 51.7% and 39.4% for the 4-view and 8-view configurations, respectively, as measured by the ADD metric. With the availability of depth data, the performance of “CosyPose+LINE2D” shows substantial improvement, representing its upper bound. In contrast, our method exceeds this upper bound by a clear margin, achieving detection rates that are 13.0% and 7.2% higher on the 4-view and 8-view test sets, respectively, with the ADD metric. A similar margin is observed when using the  $(5\text{ mm}, 10^\circ)$  metric.

In the RealSense test set, the degraded quality of depth data presents challenges for both the “MV-3D-KP” and “CosyPose+LINE2D” (RGB-D version) methods. In contrast and as expected, our approach maintains a comparable detection rate. Specifically, for the 4-view configuration, our approach exhibits only a slight decrease in performance compared to the “MV-3D-KP” by 1.8% and 6.7% using the ADD and the  $(5\text{ mm}, 10^\circ)$  metric. With the 8-view configuration, our approach achieves the best performance of 90.1% using the ADD metric and 76.8% using the  $(5\text{ mm}, 10^\circ)$  metric, respectively.

### 5.4 Results on T-ROBI Dataset

Table 3 presents the object pose estimation results on our T-ROBI dataset, where our approach demonstrates clear superiority. It significantly outperforms “CosyPose” (all variants) and “MV-3D-KP” by a substantial margin. Using the ADD metric, our method demonstrates an impressive overall detection rate of 93.4% for the 4-view configuration and 95.2% for the 8-view configuration. When evaluated with the  $(5\text{ mm}, 10^\circ)$  metric, it achieves detection rates of 79.4% with 4 views and 81.3% with 8 views, highlighting its robustness in handling transparent objects. In contrast, the “MV-3D-KP” and “CosyPose+LINE2D” (RGB-D version) approaches show low detection rates, largely due to significant depth missing and inaccuracies.

### 5.5 Ablation Studies on Pose Estimation

We conduct ablation studies to evaluate the effect of using the edge map and the decoupled formulation on the ROBI and T-ROBI dataset. Table 4 summarizes the results of our ablation studies.

Object Edge	Decoupled Formulation	ADD		(5 mm, 10°)		Run-time (ms)
		4 Views	8 Views	4 Views	8 Views	
×	×	70.3	78.4	48.3	55.4	157.2
×	✓	73.3	79.7	48.5	55.8	<b>34.1</b>
✓	×	85.4	90.1	71.9	78.6	197.7
✓	✓	<b>86.5</b>	<b>91.2</b>	<b>72.1</b>	<b>79.3</b>	48.5

**Table 4.** Ablation studies on different configurations for the 6D object pose estimation on the **ROBI** and **T-ROBI** datasets. The reported results represent the detection rate based on the ADD and 5-mm/10-degree metrics. **Object Edge** refers to utilizing the object’s 2D edge map, predicted by the MEC-Net, to obtain per-frame object orientation measurements. **Decoupled Formulation** presents the results of our method when the 6D object pose estimation is decomposed into a sequential two-step process. We conduct the run-time analysis for **estimating per-frame orientation measurement using LINE-2D** and report with milliseconds per object. The analysis is conducted on a laptop with an Intel 2.60GHz CPU.

**Edge Map.** As presented in Section 3.3, for optimizing the object 3D orientation, we use a template matching-based orientation estimator, LINE-2D, to obtain the per-frame object orientation measurement. However, LINE-2D is susceptible to issues related to occlusion and fake edges. Compared to our previous approach (Yang et al. 2023b), we address these problems by leveraging our MEC-Net to directly produce the object’s 2D edge map. To demonstrate the advantage of this approach, we conduct a comparison of the final results with and without using the edge map. In cases where edge maps are unavailable, we take the object mask from the MEC-Net and then feed the re-cropped object RoI into the LINE-2D estimator. Table 4 clearly shows a significant increase in the correct detection rate when utilizing the estimated edge map. This phenomenon is more obvious when using the metric, (5 mm, 10°), which imposes a stricter criterion for orientation error.

**Decoupled Formulation.** As discussed in Section 3.1 and 3.3.1, the core idea of our method is the decoupling of 6D pose estimation into a sequential two-step process. This process first resolves the scale and depth ambiguities in the RGB images and greatly improves the orientation estimation performance. To justify its effectiveness, we consider an alternative version of our approach, one which simultaneously estimates the 3D translation and orientation. This version uses the same strategy to estimate the object translation. However, instead of using the provided scale from the translation estimates, it uses the multi-scale trained templates (similar to the RGB version of CosyPose) to acquire orientation measurements. Table 4 shows that, due to the large number of templates, the run-time for orientation

estimation is generally slow for the simultaneous process version. In comparison, our two-step process not only operates with a much faster run-time speed but also has slightly better overall performance.

## 5.6 Next-Best-View Evaluation

For evaluation, we compare our next-best-view approach against two heuristic-based approaches, “Random” and “Max-Distance” as the baselines. For all view selection strategies, we use our object pose estimation approach for a fair comparison. To obtain the results, we initialize the object pose estimation with 2 viewpoints and set the maximum number of additional viewpoints to 2 (a total of 4 viewpoints are used). As shown in Table 5, comparing to the “Random” and “Max-Distance” baselines, our method outperforms them by a margin of at least 1.2% with the ADD metric and 1.3% with the 5-mm/10-degree metric, respectively.

Figure 12 further presents NBV results on ROBI and T-ROBI dataset when using different number of viewpoints with the ADD metric. We can see that to achieve the same level of correct detection rate, our NBV policy (blue curve) requires fewer viewpoints than the “Random” (red curve) and “Max-Distance” baseline (green curve).

## 6 CONCLUSION

In this work, we present a complete framework of multi-view pose estimation and next-best-view prediction for textureless objects. For our multi-view object pose estimation approach, the core idea of our method is to decouple the posterior distribution into a 3D translation and a 3D orientation of

Metrics\Objects		Tube Fitting	Chrome Screw	Eye Bolt	Gear*	Zigzag	DIN Connector	D-Sub Connector†	Bottle	Pipe Fitting	ALL
ADD	Random	85.8	82.4	90.7	92.3	95.3	71.1	80.7	94.2	96.4	87.0
	Max	<b>89.5</b>	<b>87.7</b>	92.6	96.6	96.5	72.2	82.8	<b>96.1</b>	96.4	90.1
	NBV	89.0	87.3	<b>94.4</b>	<b>98.3</b>	<b>97.7</b>	<b>76.7</b>	<b>83.7</b>	<b>96.1</b>	<b>98.2</b>	<b>91.3</b>
(5, 10)	Random	80.4	82.0	52.8	87.2	90.7	<b>53.9</b>	44.6	71.2	87.5	72.7
	Max	<b>84.5</b>	84.0	66.7	<b>94.0</b>	90.7	52.2	46.8	<b>82.7</b>	87.5	76.5
	NBV	82.2	<b>84.4</b>	<b>74.1</b>	93.2	<b>95.4</b>	52.2	<b>51.1</b>	78.8	<b>89.3</b>	<b>77.8</b>

\*In our evaluation, we treat the object “Gear” as symmetric about the Z-axis with an order of 12.

†In our evaluation, we treat the object “D-Sub Connector” as symmetric about the Z-axis with an order of 2.

**Table 5.** Next-Best-View evaluation. We show the object pose estimation results with different viewpoint selection strategies on the full **ROBI** and **T-ROBI** dataset, expressed as the correct detection rate. An object pose is considered correct if it lies within the ADD or (5 mm, 10°) metric. We initialize the object pose estimation with two viewpoints. The maximum number of additional viewpoints is set to two (a total of four viewpoints).

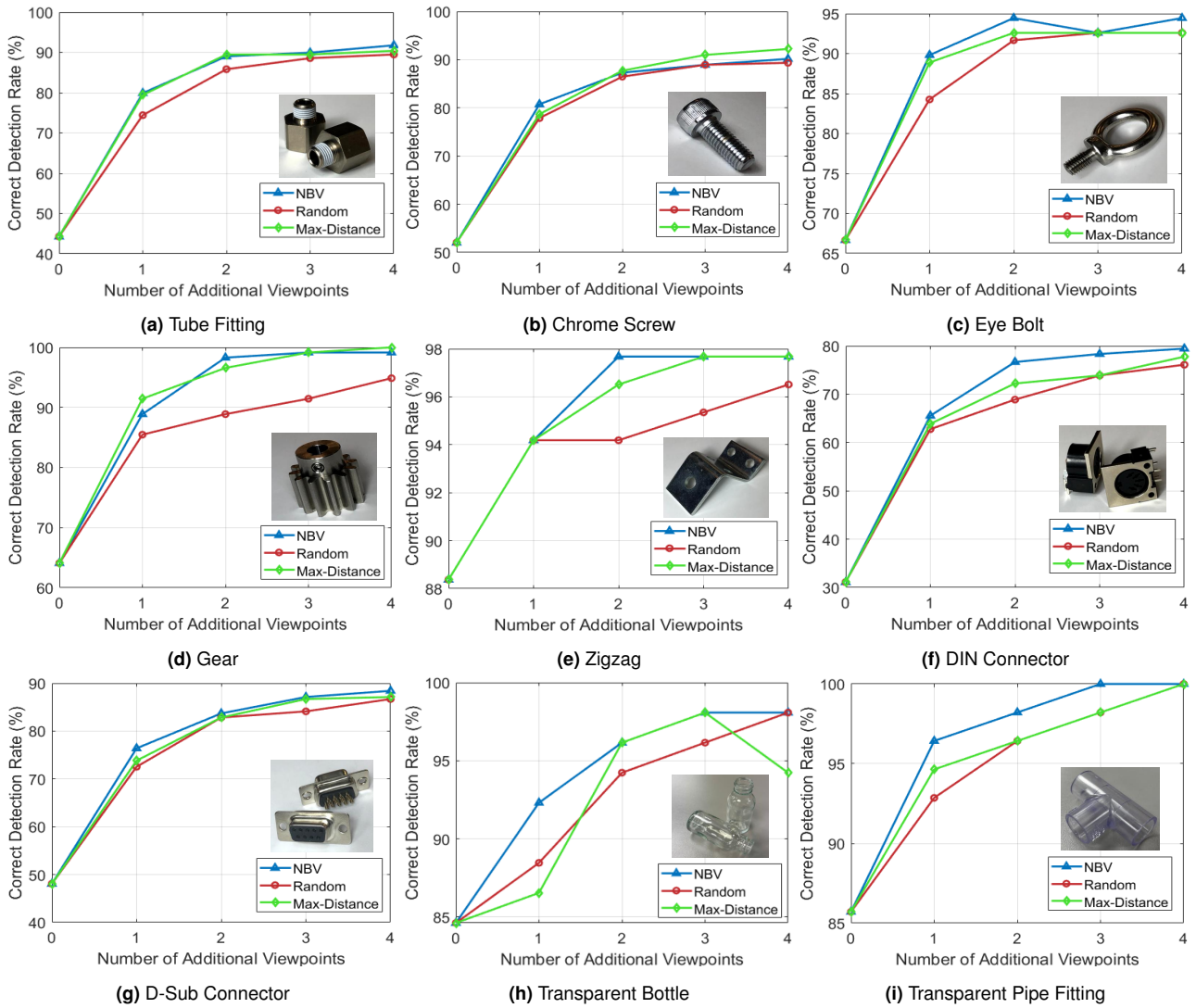


**Figure 12.** Evaluation of our next-best-view policy when comparing against heuristic-based baselines. We use our multi-view pose estimation approach for all the viewpoint selection strategies. The results are evaluated using the correct detection rate with the ADD metric on the Ensenso test set. Our approach can achieve a high correct detection rate with fewer viewpoints.

an object and integrate the per-frame measurements with a two-step multi-view optimization formulation. This process first resolves the scale and depth ambiguities in the RGB images and greatly simplifies the per-frame orientation estimation problem. Moreover, our orientation optimization module explicitly handles the object symmetries and counteracts the measurement uncertainties with a max-mixture-based formulation. To find the next-best-view, we predict the object pose entropy via the Fisher information approximation. The new RGB measurements are collected from the corresponding viewpoint to improve the object pose accuracy. Experiments on the real-world ROBI and our transparent dataset demonstrate the effectiveness and accuracy compared to the state-of-the-art baselines. As a future work, we look to investigate how to jointly estimate both object poses and camera poses, and explore how to extend our active perception formulation to CAD-less objects.

## References

- AESUB (2025) Aesub blue: Vanishing 3d scanning spray. <https://aesub.com>.
- Aloimonos J, Weiss I and Bandyopadhyay A (1988) Active vision. *International Journal of Computer Vision* 1(4): 333–356.
- Bajcsy R, Aloimonos Y and Tsotsos JK (2018) Revisiting active perception. *Autonomous Robots* 42(2): 177–196.
- Brachmann E, Michel F, Krull A, Yang MY, Gumhold S and Gumhold S (2016) Uncertainty-driven 6d pose estimation of objects and scenes from a single rgb image. In: *IEEE/CVF Conference on Computer Vision and Pattern recognition (CVPR)*.
- Breyer M, Ott L, Siegwart R and Chung JJ (2022) Closed-loop next-best-view planning for target-driven grasping. In: *IEEE/RSJ International Conference on Intelligent Robots and Systems (IROS)*.
- Bui M, Zakharov S, Albarqouni S, Ilic S and Navab N (2018) When regression meets manifold learning for object recognition and pose estimation. In: *IEEE International Conference on Robotics and Automation (ICRA)*.



- Cai D, Heikkilä J and Rahtu E (2022) Ove6d: Object viewpoint encoding for depth-based 6d object pose estimation. In: *IEEE/CVF Conference on Computer Vision and Pattern recognition (CVPR)*.
- Chai CY, Wu YP and Tsao SL (2020) Deep depth fusion for black, transparent, reflective and texture-less objects. In: *IEEE International Conference on Robotics and Automation (ICRA)*.
- Chen K, James S, Sui C, Liu YH, Abbeel P and Dou Q (2023) Stereopose: Category-level 6d transparent object pose estimation from stereo images via back-view nocs. In: *IEEE International Conference on Robotics and Automation (ICRA)*.
- Chen S, Li Y and Kwok NM (2011) Active vision in robotic systems: A survey of recent developments. *International Journal of Robotics Research* 30(11): 1343–1377.
- Choi CL, Xu B and Leutenegger S (2023) Accurate and interactive visual-inertial sensor calibration with next-best-view and next-best-trajectory suggestion. In: *IEEE/RSJ International Conference on Intelligent Robots and Systems (IROS)*.
- Collet A and Srinivasa SS (2010) Efficient multi-view object recognition and full pose estimation. In: *IEEE International Conference on Robotics and Automation (ICRA)*.
- Community BO (2018) *Blender-a 3D modelling and rendering package*. Blender Foundation, Stichting Blender Foundation, Amsterdam. URL <http://www.blender.org>.
- Connolly C (1985) The determination of next best views. In: *IEEE International Conference on Robotics and Automation (ICRA)*.
- Coumans E and Bai Y (2016) Pybullet, a python module for physics simulation for games, robotics and machine learning .
- Davison AJ and Murray DW (2002) Simultaneous localization and map-building using active vision. *IEEE Transactions on Pattern Analysis and Machine Intelligence* 24(7): 865–880.
- Deng X, Mousavian A, Xiang Y, Xia F, Bretl T and Fox D (2021) Poserbpf: A rao–blackwellized particle filter for 6-d object pose tracking. *IEEE Transactions on Robotics* 37(5): 1328–1342.
- Deng X, Xiang Y, Mousavian A, Eppner C, Bretl T and Fox D (2020) Self-supervised 6d object pose estimation for robot manipulation. In: *IEEE International Conference on Robotics and Automation (ICRA)*.
- Doumanoglou A, Kouskouridas R, Malassiotis S and Kim TK (2016) Recovering 6d object pose and predicting next-best-view in the crowd. In: *IEEE/CVF Conference on Computer Vision and Pattern recognition (CVPR)*.
- Drost B, Ulrich M, Navab N and Ilic S (2010) Model globally, match locally: Efficient and robust 3d object recognition. In: *IEEE Computer Society Conference on Computer Vision and Pattern Recognition*.
- Eidenberger R and Scharinger J (2010) Active perception and scene modeling by planning with probabilistic 6d object poses. In: *IEEE/RSJ International Conference on Intelligent Robots and Systems (IROS)*.
- Forster C, Pizzoli M and Scaramuzza D (2014) Appearance-based active, monocular, dense reconstruction for micro aerial vehicles. In: *Robotics: Science and Systems (RSS)*.
- Fu J, Huang Q, Doherty K, Wang Y and Leonard JJ (2021) A multi-hypothesis approach to pose ambiguity in object-based slam. In: *IEEE/RSJ International Conference on Intelligent Robots and Systems (IROS)*.
- Gao G, Lauri M, Hu X, Zhang J and Frntrop S (2021) Cloudaae: Learning 6d object pose regression with on-line data synthesis on point clouds. In: *IEEE International Conference on Robotics and Automation (ICRA)*.
- Gao G, Lauri M, Wang Y, Hu X, Zhang J and Frntrop S (2020) 6d object pose regression via supervised learning on point clouds. In: *IEEE International Conference on Robotics and Automation (ICRA)*.
- Haugaard RL and Buch AG (2022) Surfemb: Dense and continuous correspondence distributions for object pose estimation with learnt surface embeddings. In: *IEEE/CVF Conference on Computer Vision and Pattern recognition (CVPR)*.
- Haugaard RL and Iversen TM (2023) Multi-view object pose estimation from correspondence distributions and epipolar geometry. In: *IEEE International Conference on Robotics and Automation (ICRA)*.
- He K, Zhang X, Ren S and Sun J (2016) Deep residual learning for image recognition. In: *IEEE/CVF Conference on Computer Vision and Pattern recognition (CVPR)*.
- He Y, Sun W, Huang H, Liu J, Fan H and Sun J (2020) Pvn3d: A deep point-wise 3d keypoints voting network for 6dof pose estimation. In: *IEEE/CVF Conference on Computer Vision and Pattern recognition (CVPR)*.
- He Z, Li Q, Zhao X, Wang J, Shen H, Zhang S and Tan J (2023) Contourpose: Monocular 6-d pose estimation method for reflective textureless metal parts. *IEEE Transactions on Robotics* 39(5): 4037–4050.
- Hinterstoisser S, Cagniart C, Ilic S, Sturm P, Navab N, Fua P and Lepetit V (2011) Gradient response maps for real-time detection of textureless objects. *IEEE Transactions on Pattern Analysis and Machine Intelligence* 34(5): 876–888.
- Hinterstoisser S, Lepetit V, Ilic S, Holzer S, Bradski G, Konolige K and Navab N (2012) Model based training, detection and pose estimation of texture-less 3d objects in heavily cluttered scenes. In: *Asian Conference on Computer Vision (ACCV)*.
- Hodan T, Barath D and Matas J (2020) Epos: Estimating 6d pose of objects with symmetries. In: *IEEE/CVF Conference on Computer Vision and Pattern recognition (CVPR)*.
- Hodaň T, Zabulis X, Lourakis M, Obdržálek Š and Matas J (2015) Detection and fine 3d pose estimation of texture-less objects in rgb-d images. In: *IEEE/RSJ International Conference on Intelligent Robots and Systems (IROS)*.
- Huber MF, Bailey T, Durrant-Whyte H and Hanebeck UD (2008) On entropy approximation for gaussian mixture random vectors. In: *IEEE International Conference on Multisensor Fusion and Integration for Intelligent Systems*.
- IDS (2025) Ensenso 3d camera. <https://www.ensenso.com/>.
- Imperoli M and Pretto A (2015) D2co: Fast and robust registration of 3d textureless objects using the directional chamfer distance. In: *International Conference on Computer Vision Systems (ICVS)*.
- Islar S, Sabzevari R, Delmerico J and Scaramuzza D (2016) An information gain formulation for active volumetric 3d reconstruction. In: *IEEE International Conference on Robotics and Automation (ICRA)*.
- Kehl W, Manhardt F, Tombari F, Ilic S and Navab N (2017) Ssd-6d: Making rgb-based 3d detection and 6d pose estimation great again. In: *IEEE/CVF International Conference on Computer Vision (ICCV)*.

- Kingma D and Ba J (2015) Adam: A method for stochastic optimization. In: *International Conference on Learning Representations (ICLR)*. San Diego, CA, USA.
- Klein G and Murray D (2007) Parallel tracking and mapping for small ar workspaces. In: *IEEE/ACM International Symposium on Mixed and Augmented Reality*.
- Kundu JN, Rahul M, Ganeshan A and Babu RV (2018) Object pose estimation from monocular image using multi-view keypoint correspondence. In: *European Conference on Computer Vision (ECCV)*.
- Labbé Y, Carpentier J, Aubry M and Sivic J (2020) Cosypose: Consistent multi-view multi-object 6d pose estimation. In: *European Conference on Computer Vision (ECCV)*.
- Lepetit V, Moreno-Noguer F and Fua P (2009) Epnp: An accurate o(n) solution to the pnp problem. *International Journal of Computer Vision* 81(2): 155–166.
- Li A and Schoellig AP (2023) Multi-view keypoints for reliable 6d object pose estimation. In: *IEEE International Conference on Robotics and Automation (ICRA)*.
- Li Y, Wang G, Ji X, Xiang Y and Fox D (2018) Deepim: Deep iterative matching for 6d pose estimation. In: *European Conference on Computer Vision (ECCV)*.
- Li Z and Stamos I (2023) Depth-based 6dof object pose estimation using swin transformer. In: *IEEE/RSJ International Conference on Intelligent Robots and Systems (IROS)*.
- Liao Z, Yang J, Qian J, Schoellig AP and Waslander SL (2024) Uncertainty-aware 3d object-level mapping with deep shape priors. In: *IEEE International Conference on Robotics and Automation (ICRA)*.
- Liu MY, Tuzel O, Veeraraghavan A, Taguchi Y, Marks TK and Chellappa R (2012) Fast object localization and pose estimation in heavy clutter for robotic bin picking. *International Journal of Robotics Research* 31(8): 951–973.
- Liu X, Jonschkowski R, Angelova A and Konolige K (2020) Keypose: Multi-view 3d labeling and keypoint estimation for transparent objects. In: *IEEE/CVF Conference on Computer Vision and Pattern recognition (CVPR)*.
- Maninis KK, Popov S, Nießner M and Ferrari V (2022) Vid2cad: Cad model alignment using multi-view constraints from videos. *IEEE Transactions on Pattern Analysis and Machine Intelligence* 45(1): 1320–1327.
- Merrill N, Guo Y, Zuo X, Huang X, Leutenegger S, Peng X, Ren L and Huang G (2022) Symmetry and uncertainty-aware object slam for 6dof object pose estimation. In: *IEEE/CVF Conference on Computer Vision and Pattern recognition (CVPR)*.
- Morrison D, Corke P and Leitner J (2019) Multi-view picking: Next-best-view reaching for improved grasping in clutter. In: *IEEE International Conference on Robotics and Automation (ICRA)*.
- Mur-Artal R, Montiel JMM and Tardos JD (2015) Orb-slam: a versatile and accurate monocular slam system. *IEEE Transactions on Robotics* 31(5): 1147–1163.
- Olson E and Agarwal P (2013) Inference on networks of mixtures for robust robot mapping. *International Journal of Robotics Research* 32(7): 826–840.
- Park K, Patten T and Vincze M (2019) Pix2pose: Pixel-wise coordinate regression of objects for 6d pose estimation. In: *IEEE/CVF International Conference on Computer Vision (ICCV)*.
- Pavlakos G, Zhou X, Chan A, Derpanis KG and Daniilidis K (2017) 6-dof object pose from semantic keypoints. In: *IEEE International Conference on Robotics and Automation (ICRA)*.
- Peng S, Liu Y, Huang Q, Zhou X and Bao H (2019) Pvnnet: Pixel-wise voting network for 6dof pose estimation. In: *IEEE/CVF Conference on Computer Vision and Pattern recognition (CVPR)*.
- Rad M and Lepetit V (2017) Bb8: A scalable, accurate, robust to partial occlusion method for predicting the 3d poses of challenging objects without using depth. In: *IEEE/CVF International Conference on Computer Vision (ICCV)*.
- Rebello J, Das A and Waslander S (2017) Autonomous active calibration of a dynamic camera cluster using next-best-view. In: *IEEE/RSJ International Conference on Intelligent Robots and Systems (IROS)*.
- Redmon J, Divvala S, Girshick R and Farhadi A (2016) You only look once: Unified, real-time object detection. In: *IEEE/CVF Conference on Computer Vision and Pattern recognition (CVPR)*.
- Rusinkiewicz S and Levoy M (2001) Efficient variants of the icp algorithm. In: *International Conference on 3-D Digital Imaging and Modeling*.
- Saadi L, Besbes B, Kramm S and Benschrair A (2021) Optimizing rgb-d fusion for accurate 6dof pose estimation. *IEEE Robotics and Automation Letters* 6(2): 2413–2420.
- Sajjan S, Moore M, Pan M, Nagaraja G, Lee J, Zeng A and Song S (2020) Cleargrasp: 3d shape estimation of transparent objects for manipulation. In: *IEEE International Conference on Robotics and Automation (ICRA)*.
- Salas-Moreno RF, Newcombe RA, Strasdat H, Kelly PH and Davison AJ (2013) Slam++: Simultaneous localisation and mapping at the level of objects. In: *IEEE/CVF Conference on Computer Vision and Pattern recognition (CVPR)*.
- Schmidt T, Newcombe RA and Fox D (2014) Dart: Dense articulated real-time tracking. In: *Robotics: Science and Systems (RSS)*.
- Shi G, Zhu Y, Tremblay J, Birchfield S, Ramos F, Anandkumar A and Zhu Y (2021) Fast uncertainty quantification for deep object pose estimation. In: *IEEE International Conference on Robotics and Automation (ICRA)*.
- Shugurov I, Pavlov I, Zakharov S and Ilic S (2021) Multi-view object pose refinement with differentiable renderer. *IEEE Robotics and Automation Letters* 6(2): 2579–2586.
- Sock J, Garcia-Hernando G and Kim TK (2020) Active 6d multi-object pose estimation in cluttered scenarios with deep reinforcement learning. In: *IEEE/RSJ International Conference on Intelligent Robots and Systems (IROS)*.
- Song KT, Wu CH and Jiang SY (2017) Cad-based pose estimation design for random bin picking using a rgb-d camera. *Journal of Intelligent & Robotic Systems* 87: 455–470.
- Sundermeyer M, Marton ZC, Durner M, Brucker M and Triebel R (2018) Implicit 3d orientation learning for 6d object detection from rgb images. In: *European Conference on Computer Vision (ECCV)*.
- Tian M, Pan L, Ang MH and Lee GH (2020) Robust 6d object pose estimation by learning rgb-d features. In: *IEEE International Conference on Robotics and Automation (ICRA)*.
- Tremblay J, To T, Sundaralingam B, Xiang Y, Fox D and Birchfield S (2018) Deep object pose estimation for semantic robotic grasping of household objects. In: *Conference on Robot*

- Learning*.
- Tsai RY and Lenz RK (1989) A new technique for fully autonomous and efficient 3d robotics hand/eye calibration. *IEEE Transactions on Robotics and Automation* 5(3): 345–358.
- Wada K, Sucar E, James S, Lenton D and Davison AJ (2020) Morefusion: Multi-object reasoning for 6d pose estimation from volumetric fusion. In: *IEEE/CVF Conference on Computer Vision and Pattern recognition (CVPR)*.
- Wang C, Xu D, Zhu Y, Martín-Martín R, Lu C, Fei-Fei L and Savarese S (2019) Densefusion: 6d object pose estimation by iterative dense fusion. In: *IEEE/CVF Conference on Computer Vision and Pattern recognition (CVPR)*.
- Wang J, Rünz M and Agapito L (2021) Dsp-slam: Object oriented slam with deep shape priors. In: *International Conference on 3D Vision (3DV)*.
- Wu K, Ranasinghe R and Dissanayake G (2015) Active recognition and pose estimation of household objects in clutter. In: *IEEE International Conference on Robotics and Automation (ICRA)*.
- Wu Y, Zhang Y, Zhu D, Feng Y, Coleman S and Kerr D (2020) Eao-slam: Monocular semi-dense object slam based on ensemble data association. In: *IEEE/RSJ International Conference on Intelligent Robots and Systems (IROS)*.
- Xiang Y, Schmidt T, Narayanan V and Fox D (2018) Posecnn: A convolutional neural network for 6d object pose estimation in cluttered scenes. In: *Robotics: Science and Systems (RSS)*.
- Xu H, Wang YR, Eppel S, Aspuru-Guzik A, Shkurti F and Garg A (2021) Seeing glass: Joint point cloud and depth completion for transparent objects .
- Xu L, Qu H, Cai Y and Liu J (2024) 6d-diff: A keypoint diffusion framework for 6d object pose estimation. In: *IEEE/CVF Conference on Computer Vision and Pattern recognition (CVPR)*.
- Xu S, Willners JS, Hong Z, Zhang K, Petillot YR and Wang S (2023) Observability-aware active extrinsic calibration of multiple sensors. In: *IEEE International Conference on Robotics and Automation (ICRA)*.
- Yang J, Gao Y, Li D and Waslander SL (2021) Robi: A multi-view dataset for reflective objects in robotic bin-picking. In: *IEEE/RSJ International Conference on Intelligent Robots and Systems (IROS)*.
- Yang J, Rebello J and Waslander SL (2023a) Next-best-view selection for robot eye-in-hand calibration. In: *Conference on Robots and Vision (CRV)*.
- Yang J and Waslander SL (2022) Next-best-view prediction for active stereo cameras and highly reflective objects. In: *IEEE International Conference on Robotics and Automation (ICRA)*.
- Yang J, Xue W, Ghavidel S and Waslander SL (2023b) 6d pose estimation for textureless objects on rgb frames using multi-view optimization. In: *IEEE International Conference on Robotics and Automation (ICRA)*.
- Yang J, Yao J and Waslander SL (2024) Active pose refinement for textureless shiny objects using the structured light camera. In: *IEEE/RSJ International Conference on Intelligent Robots and Systems (IROS)*.
- Yang S and Scherer S (2019) Cubeslam: Monocular 3d object slam. *IEEE Transactions on Robotics* 35(4): 925–938.
- Zakharov S, Shugurov I and Ilic S (2019) Dpod: 6d pose object detector and refiner. In: *IEEE/CVF International Conference on Computer Vision (ICCV)*.
- Zhang H and Cao Q (2019) Fast 6d object pose refinement in depth images. *Applied Intelligence* 49: 2287–2300.
- Zhang Z and Scaramuzza D (2018) Perception-aware receding horizon navigation for mavs. In: *IEEE International Conference on Robotics and Automation (ICRA)*.
- Zhang Z and Scaramuzza D (2019) Beyond point clouds: Fisher information field for active visual localization. In: *IEEE International Conference on Robotics and Automation (ICRA)*.